Applied Energy 311 (2022) 118629

Contents lists available at ScienceDirect

Applied Energy

journal homepage: www.elsevier.com/locate/apenergy

# A numerical study of a taut-moored point-absorber wave energy converter with a linear power take-off system under extreme wave conditions

Bonaventura Tagliafierro [a], Iván Martínez-Estévez [b], José M. Domínguez [b], Alejandro J.C. Crespo [b,*], Malin Göteman [c], Jens Engström [c], Moncho Gómez-Gesteira [b]

[a] Department of Civil Engineering, University of Salerno, Fisciano, SA, Italy
[b] Environmental Physics Laboratory, CIM-UVIGO, Universidade de Vigo, Ourense, Spain
[c] Department of Electrical Engineering, Uppsala University, Uppsala, Sweden

ARTICLE INFO

*Keywords:*
Uppsala WEC
Embedded focused waves
NewWave
Extreme events
DualSPHysics
MoorDyn+
Project Chrono
CFD

ABSTRACT

Probably the biggest challenge for wave energy is to ensure survival in harsh offshore conditions, in order to reduce costs for offshore repair operations and downtime, and achieve economic viability. This work presents a reliable numerical tool that can be used to study the dynamics and survivability of wave energy converters in violent wave conditions, possibly cutting down the costs of experimental campaigns. Within the Smoothed Particle Hydrodynamics framework, this research identifies a detailed procedure to model a taut-moored point-absorber wave energy converter together with its inherent power take-off device, which seamlessly exploits its functions of energy harvesting and load bearing. A validation of the DualSPHysics code is provided by contrasting the numerical outcome with a thorough set of data obtained in physical tests with extreme waves, showing that the time-integrated numerical model can capture with good accuracy all the physics involved. The computational fluid dynamics tool is employed to perform a survivability study, modeling high-return period wave conditions for marine structures, and providing guidelines on how to create the numerically best setup to be used for design purposes. A real-like irregular sea state representation, comprising 500 waves, was used to draw insightful indications for the structure optimization to increase the structure's life expectancy, or conversely, to reduce the initial and operational costs.

## 1. Introduction

A point-absorber wave energy converter (WEC) consists of a floating buoy, whose wave-activated motion is converted into electricity by means of a power take-off (PTO) system [1]. Modeling of these structures should account for device kinematics, hydrodynamics, electromechanics, including different levels of details [2]. Furthermore, their potential should be evaluated when deployed in wave energy farms in which bodies are either interconnected with various technologies [3] or embedded in other systems [4], and their mutual interaction studied according to efficiency of the array layouts [5]. Due to the increased awareness of potential energy availability, offshore areas are becoming increasingly attractive for engineers and investors to implement WECs — this, however, comes at a cost of greater vulnerability to extreme events.

Thanks to knowledge transfer and to purposely developed research projects, wave energy is now on the verge of being competitive on the global market (some latest examples can be found in [6]). As PTO systems are becoming more sophisticated and complex, the investigative tools should evolve to be able to capture the whole behavior of such devices, which, in general, operate without any clear distinctions between harvesting and survival modes. Likewise, the total cost of energy often has been reduced by maximizing energy production of WECs, overly relying on simplified design practices [7], and disregarding other factors such as capital costs and *operation and maintenance* costs, which has led to seeking locations where the power carried by waves is abundant. This can lead to detrimental repercussions on the total lifetime cost, which is summarized in [8]: "there is increasing reason to believe that the first successful WECs may be better off eschewing the hunt for world's largest waves". The same concept was also expressed by [9], in which by utilizing a more comprehensive methodology for assessing the Levelized Cost of Electricity (LCoE), it is demonstrated that areas with less wave power availability can reduce the capital costs.

On the one hand, for what concerns the power production mode, practical approaches [10] and linear models are widely exploited by

* Corresponding author.
*E-mail address:* alexbexe@uvigo.es (A.J.C. Crespo).

https://doi.org/10.1016/j.apenergy.2022.118629
Received 25 October 2021; Received in revised form 30 December 2021; Accepted 24 January 2022
Available online 11 February 2022

the industry to obtain a sensible reduction in the cost of wave energy through optimization [11], that is, maximizing the energy output. This phase is conveniently dealt with by using potential flow models [12], often linear and for inviscid fluids, which can be used to reproduce the response of WECs under operational sea states. Potential flow-based models comprise a vast variety of solutions (see, for example, [13,14], and [15]), providing fast and relatively accurate answers suitable for investigating performance within serviceability limit states (SLS); however, they do require assumptions to include viscous effects and wave superposition. Some authors have pointed out the great limitations of such approaches [16], issuing several warnings on their use for analyses where highly non-linear interactions take place [7]; however, they can be skillfully used to pinpoint with more precision the conditions (combinations of factors) that are more likely to produce certain scenarios [17].

Structures with significant dynamic response require stochastic modeling of the sea surface and its kinematics by time series, entailing the use of time-domain analyses. Real sea states are best described by irregular wave models, either linear or non-linear. On top of this, other environmental conditions such as wind, tides, and currents can affect the magnitude of the corresponding loads. Unless a tailored design procedure is identified for each specific WEC, it is generally prescribed to use a time-domain simulation of at least three hours to completely represent an extreme event, containing approximately 1000 waves [18], thus providing a statistically treatable significant series of datum points. However, the length of the series is strongly dependent on the quantity being investigated and the nature of failure (e.g., fatigue analysis) [19]. Certain applications may be reliable enough with 300 waves [20], however there is not yet a general rule.

Unfortunately, identifying the conditions that are likely to produce the maximum effects (loads) will require a full understanding of how winds, waves, and currents impact on the system dynamics and subsequently the loads. Within a stochastic framework [21], the environmental variables should be combined, using combinations of their expected values according to their probability of occurring simultaneously. As such, for a system with a large number of degrees of freedom, the number of combinations may well go to the hundreds, hampering the straightforward use of computationally expensive CFD simulations. Approaching the solution of this problem through physical testing is not an option either, for the system would lack any flexibility to respond to combined environmental actions (e.g., waves and currents) and/or changes in the structural configuration (e.g., a damaged connection). Presently, the best way to tackle this problem is through a multi-tier design procedure [22], which may start with linear approaches and frequency-domain analyses, and then proceed with mid-fidelity simulations to narrow the range of environmental conditions [17,23].

Survivability analyses, on the other hand, need more complex and sophisticated models that can guaranteeing high-fidelity modeling procedures in order to solve the dynamics of the system as a whole. For handling WEC simulations, CFD (Computational Fluid Dynamics) methods represent the best option: they do not require heavy preventive assumptions on the fluid mechanics, solving the fluid motion by means of the Navier–Stokes equations in spatial domain and in time, and either meshbased or mesh-less approach can be used (see [24]). Several examples of WEC simulations using CFD frameworks have proven the viability of this approach when the PTO apparatus is also included, following a variety of models (for example, [25–27], or [28]). The significant limitation of the use of CFD tools for the design phases of WECs is their computational cost.

Regardless of the scenario, for CFD simulations of WECs, the Smoothed Particle Hydrodynamics (SPH) method represents a viable approach [24] with the appropriate degree of flexibility in reproducing moving objects under violent fluid motion [29], overcoming mesh distortion issues presented by mesh-based solvers. Nevertheless, few applications can be found in the literature as reviewed in [29,30]. Here, the open-source DualSPHysics code [31], based on the SPH method, becomes a suitable option. Its highly parallelized structure harnesses the computing power of graphics processing unit (GPU) cards, allowing for a speed-up up to 100 when compared with CPU calculations, and has demonstrated accuracy equivalent to well-known meshbased models [32]. Thanks to the coupling with the Project Chronov [33] and MoorDyn+ libraries (based on MoorDyn [34]), the DualSPHysics framework can embed multi-featured complex mechanisms typically deployed in WECs, such as the features of the WEC under study in this work. DualSPHysics has been proven to simulate with accuracy a great variety of WECs: an oscillating wave surge converter with mechanical constraints was validated in [35] under regular wave conditions; complete dynamic investigations of heaving point absorbers [26,36–38]; and fixed oscillating water column devices have been studied [39,40].

The Uppsala WEC [41] has been considered as a reference case in this research; it operates according to the principles that hold for floating oscillating body devices, which are mainly designed to operate offshore (often in deep-water conditions). The concept was devised in the early 2000s and installed for the first pilot wave power plants deploying this technology [41]; it was physically tested under constrained focused waves and irregular waves in [42]. The device has been used ever since as a benchmark for numerical model validation, including consideration of the electromechanics of the PTO. Table 1 reports on the body of research that has leveraged the Uppsala WEC concept to widen understanding of the economic viability of moored point absorbers, expanding upon the previous background for extreme wave modeling [43]. All the pieces of research utilized mesh-based CFD software (i.e., OpenFOAM, IHFOAM and ANSYS Fluent) to investigate the performance of the Uppsala WEC under various extreme wave conditions.

However, the software that has complemented the experimental investigation needs highly skilled operators (OpenFOAM, IHFOAM) due to the modification in the source code to model the dynamics of the linearly-constrained PTO and the mooring line. Furthermore, despite the progress made in recent years, mesh-based CFD software is often challenged by simulations that entail the use of costly overset mesh for solving violent wave conditions [7,16,47]. Developing and validating new, reliable numerical simulation methods based on meshfree methods is of utmost importance.

This work proposes, for the first time, the application of an SPH-based model for the Uppsala WEC model. The proposed CFD software overcomes the above-mentioned problems by being fully integrated with two external libraries for simulating mechanical systems (e.g., linear PTOs) and mooring lines, and by being mesh-less. The DualSPHysics code is used to study a taut-moored point-absorber WEC with a linear PTO system under extreme wave conditions, investigating the various quantities that are vital for the Ultimate-Limit State (ULS) safety checks of this type of structures under high return-period events. The paper is arranged as follows: Section 2 describes in detail the basics of the mathematical foundation of the SPH method and its implementation in the code distribution herein used; Section 3 presents the code augmentation achieved through coupling techniques that allow leveraging specialized libraries within the same framework; Sections Section 4 presents the experimental setup for the Uppsala WEC whereas Section 5 describes the numerical configuration and proposes a general procedure for reproducing similar devices as well, in particular PTO calibrations; Section 6 validates the numerical model, for two distinct PTO configurations, under embedded focused waves. Finally, Section 7 presents long time series CFD simulations representing a real sea-state condition with 500 waves that impact the Uppsala WEC. Section 8 closes this work by synthesizing the main achievements.

## 2. DualSPHysics code

### 2.1. SPH basis

The SPH method is mathematically built up on a convolution integral approximation: any function $F$ can be defined by:

$$F(\boldsymbol{r}) = \int F(\boldsymbol{r}')W(\boldsymbol{r}-\boldsymbol{r}')\mathrm{d}\boldsymbol{r}', \tag{1}$$

**Table 1**
Research papers reporting on the numerical hydrodynamics performance of the Uppsala University WEC under various scenarios.

| Reference | Numerical model | Validation with | Type of waves | Validated data | Scope |
|---|---|---|---|---|---|
| [44] | VOF-RANS (OpenFOAM) | Exp. | Regular and focused waves | Incident wave, Motion, Line force | Survivability |
| [25] | Analytical, VOF-RANS (OpenFOAM and ANSYS Fluent) | EXP | Regular and focused waves | Motion, Line force | Survivability |
| [45] | BEM, VOF-RANS (ANSYS Fluent) | EXP and NUM | Irregular waves | Incident wave, Motion, Line force | Survivability under irregular waves |
| [46] | VOF-RANS (OpenFOAM) | EXP | Regular and focused waves | Motion, Line force | Survivability under tsunami waves |
| [28] | VOF-RANS (IHFOAM) | EXP | Focused waves | Motion, Line force | Survivability with focused waves |

BEM: Boundary Element Method; VOF-RANS: Volume of Fluid-Reynolds-averaged Navier–Stokes' (equations); EXP: Experiments; NUM: Numerical data.

where $W$ is the kernel function [48], $\boldsymbol{r}$ is the position vector of the point where the function is being computed, $\boldsymbol{r}'$ is the position vector of another computational point (or particle). The function $F$ is approximated by interpolating particle contributions; a summation is performed all over the particles within the compact support of the kernel:

$$F(\boldsymbol{r_a}) \approx \sum_b F(\boldsymbol{r_b}) W(\boldsymbol{r_a} - \boldsymbol{r_b}, h) \frac{m_b}{\rho_b}, \tag{2}$$

where $a$ is the interpolated particle, $b$ is a neighboring particle, $m$ and $\rho$ being the mass and the density, respectively, $m_b/\rho_b$ the volume associated with the neighboring particle $b$, and $h$ is the smoothing length. For the sake of consistency, the kernel function $W$ must fulfill several properties, such as positivity on the compact support, normalization, and monotonically decreasing with distance [49]. The weighting function used in this work is the piecewise polynomial Quintic Wendland (QW) kernel [50]:

$$W(q) = \alpha_D \left(1 - \frac{q}{2}\right)^4 (2q+1), \quad \text{with:} \quad 0 \le q \le 2, \tag{3}$$

where $\alpha_D$ is a real number that ensures the kernel normalization property:

$$\int W(|\boldsymbol{r} - \boldsymbol{r}'|) d\boldsymbol{r}' = 1,$$

$q = r/h$ is the non-dimensional distance between particles, $r$ is the distance between a certain particle $a$ and another particle $b$, and

$$h = 1.20\sqrt{3} dp$$

is the smoothing length in which $dp$ is the initial inter-particle spacing. In this work, the QW kernel is used to compute interactions of particles at a distance up to the value of $2h$.

### 2.2. Governing equations

In fluid mechanics, the SPH method is used to discretize a volume of fluid as a set of particles and the Navier–Stokes (N–S) equations dictate their motion. In the Lagrangian framework, the differential form of momentum N–S Eqs. (4) and the continuity Eq. (5) can be written in their discrete version using the kernel function:

$$\frac{d\boldsymbol{v_a}}{dt} = -\sum_b m_b \left(\frac{P_a + P_b}{\rho_a \rho_b} + \Pi_{ab}\right) \nabla_a W_{ab} + \boldsymbol{g}, \tag{4}$$

$$\frac{d\rho_a}{dt} = \rho_a \sum_b \frac{m_b}{\rho_b} \boldsymbol{v}_{ab} \nabla_a W_{ab} + 2\delta hc \sum_b (\rho_b - \rho_a) \frac{\boldsymbol{v}_{ab} \nabla_a W_{ab}}{\boldsymbol{r}_{ab}^2} \frac{m_b}{\rho_b}, \tag{5}$$

where $t$ is the time, $\boldsymbol{v}$ is the velocity, $P$ pressure, $\boldsymbol{g}$ is the gravitational acceleration, $\nabla_a$ is the gradient operator, $W_{ab}$ the kernel function, whose value depends on the distance between $a$ and $b$, $\delta$ is a parameter that governs the diffusive term, $\boldsymbol{r}_{ab} = \boldsymbol{r}_a - \boldsymbol{r}_b$ with $\boldsymbol{r}_k$ being the position of the particle $k$, and $c$ is the speed of sound.

The artificial viscosity term, $\Pi_{ab}$, is added in the momentum equation based on the Neumann–Richtmeyer artificial viscosity, aiming to reduce oscillations and stabilize the SPH scheme, following the work of [49]. In addition, the term $\delta$ controls the density diffusion term (last term in Eq. (5)) that is implemented in DualSPHysics, which works as a high frequency numerical noise filter improving the stability of the scheme by smoothing the density. The formulation is based on the density diffusion terms introduced by [51] and further developed under the name of *delta-SPH* in [52]. For the simulations performed in this work, the second term in the right-hand side of the continuity Eq. (5) is solved according to the formulation proposed in [53], which considers the only the dynamic density to control the intensity of the diffusive term.

A relationship between density and pressure bonds the system of equations. DualSPHysics uses a weakly compressible SPH formulation (WCSPH) for modeling Newtonian fluids and, for such formulation, Tait's equation of state is used to determine fluid pressure, $P$, from particle density. Following [54], it can be expressed as [55]:

$$P = \frac{c^2 \rho_0}{\gamma} \left(\left(\frac{\rho}{\rho_0}\right)^\gamma - 1\right), \tag{6}$$

where $\rho_0$ is the reference fluid density, $\gamma$ is the polytropic constant. The fluid compressibility is adjusted so that $c$ can be artificially lowered to assure reasonable values for the timesteps.

### 2.3. Rigid body dynamics and SPH

A full SPH model can deal with rigid bodies by computing the total force contributions of the surrounding fluid. In DualSPHysics, the motion of objects interacting with fluid particles is handled by the basic equations of rigid body dynamics. The geometries of these objects are discretized by filling the volume they occupy with boundary particles; for those particles it is assumed that they behave following the dynamics of each body's center of mass. Each boundary particle $k$ experiences a force per unit mass given by:

$$\boldsymbol{f}_k = \boldsymbol{g} + \sum_{b \in \text{fluid}} \boldsymbol{f}_{kb}. \tag{7}$$

$\boldsymbol{f}_{kb}$ is the force per unit mass exerted by the fluid particle $b$ on the boundary particle $k$. For the motion of a rigid body, the basic equations of rigid body dynamics can then be used:

$$\boldsymbol{M} \frac{d\boldsymbol{V}}{dt} = \sum_{k \in \text{body}} m_k \boldsymbol{f}_k, \tag{8}$$

$$\boldsymbol{I} \frac{d\boldsymbol{\Omega}}{dt} = \sum_{k \in \text{body}} m_k (\boldsymbol{r}_k - \boldsymbol{r}_0) \times \boldsymbol{f}_k, \tag{9}$$

where $\boldsymbol{M}$ is the matrix mass of the object, $\boldsymbol{I}$ is the matrix moment of inertia, $\boldsymbol{V}$ is the velocity, $\boldsymbol{\Omega}$ the angular velocity, and $\boldsymbol{r}_0$ the center of mass; $\times$ indicates the cross product. Eqs. (8) and (9) are integrated in time to predict the values of $\boldsymbol{V}$ and $\boldsymbol{\Omega}$ at the beginning of the next time step. Each boundary particle within the body has a velocity given by:

$$\boldsymbol{v_k} = \boldsymbol{V} + \boldsymbol{\Omega} \times (\boldsymbol{r_k} - \boldsymbol{r_0}). \tag{10}$$

Finally, the boundary particles within each rigid body are moved by integrating Eq. (10) in time. This approach has been checked out by [56], which shows that linear and angular momentum are conservative properties. Validations about buoyancy-driven motion are performed in [57], where DualSPHysics is tested for solid objects larger than the smallest flow scales and with various densities; [58] provides a validation for the motion of a freely floating box under linear waves.

### 2.4. Modified dynamic boundary conditions

DualSPHysics implements the Dynamic Boundary Condition (DBC), proposed by [59], as a standard method for the definition of the boundary conditions. The DBC treatment has demonstrated to work properly when applied to cases of wave propagation and wave run-up of armor block breakwaters with complex geometries [60]. However, a novel formulation was proposed by [61] in order to improve the initial DBC formulation, eliminating the creation of large gaps when the transition from non-wet to wet bounds takes place.

The modification of DBCs (the so-called mDBCs) works with the same particle arrangement defined for its parent version, but the interacting boundary surface is located between the outermost particle layers of the body and the fluid domain. Once the geometry has been characterized by normal vectors, this latter location is used to mirror ghost nodes into the fluid domain and hence evaluating the fluid properties at that virtual position; eventually, these properties are used to correct the SPH approximation when a fluid particle interacts with an mDBC particle, as it was already performed in [62,63].

## 3. Coupling with external libraries

Multyphysics simulations rely on coupling strategies between different pieces of software to create a unique environment in which different differential systems of equations are separately solved. This strategy is implemented in DualSPHysics by creating a fully Lagrangian 3D *world* that contains the geometry for the whole system. As discussed, the fluid phase is managed by the internal SPH solver described in Section 2; the dynamics of rigid bodies, comprising also the solid–solid contacts, is managed by the Project Chrono library [33], whereas the effects of mooring lines on floating structures is addressed by the MoorDyn+ library [64]. Mooring lines are vital for offshore structures (some examples can be found in [65,66]) for their capability of providing connections spanning long distances; their small usage of material is due to a combination of high-resistance material and the absence of bending-induced stress. These features are indeed needed to reproduce the response of PTO systems and to account for the various connectivity among the parts of WECs, and/or of WEC arrays.

### 3.1. Coupling with project Chrono library

The Project Chrono library has been implemented into the original DualSPHysics framework, creating an integrated interface for simulating structure–structure interaction as well [67]. The library is primarily developed to handle very large systems of 3D rigid bodies [68], with interactions among them. The coupling allows for arbitrarily shaped bodies to be considered, and the solver can integrate externally applied forces and torques, and the effects of kinematic-type restrictions, dynamic-type restrictions. Appendix A provides a description of the contact tracing method and of the spring–damper element, which are the functions utilized in this study.

### 3.2. Coupling with MoorDyn+

The two-way coupling presented in [58] is used for the simulations in this work. The open-source MoorDyn+ library solves the mooring dynamics using the lumped-mass approach inherited from the first version of MoorDyn [34]. An exhaustive description of the theory implemented for this work is presented in Appendix B.

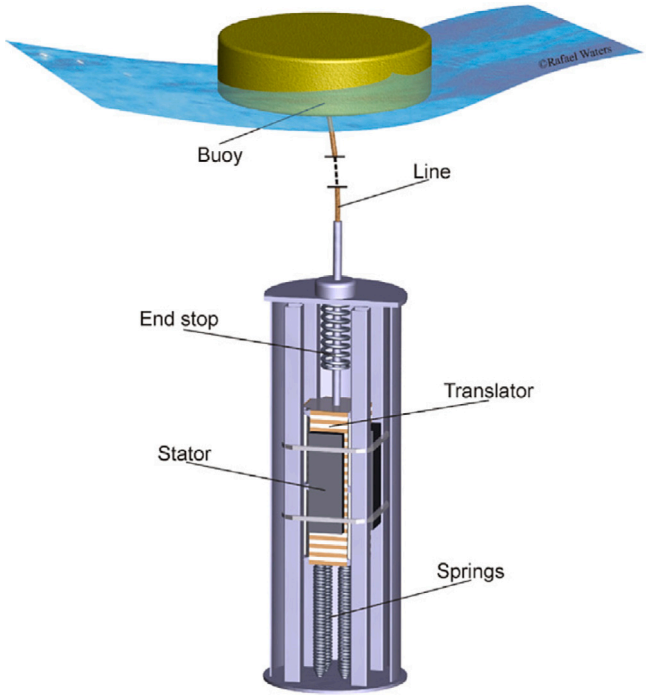


**Fig. 1.** Schematic of the Uppsala WEC [41] with a cylinder buoy. The various components of the PTO systems are tagged according to the function they are designed for.
*Source:* [25].

## 4. Experimental setup

A 1/20th-scale model WEC (Froude similarity) was studied in a wave tank in [42], with features reminiscent of the Uppsala WEC. For the validation proposed in this work, the setup that made use of a cylindrical float (refer to Fig. 1) is chosen. The buoy is taut-moored to a mass that is constrained to move only along the vertical direction; a line connects the buoy with the translator. As opposed to the mainstream rotating generators, in fact, the Uppsala WEC proposes a linear generator directly driven from the rectified motion of a floating buoy. The relative motion between the *translator* and the *stator* produces a moving magnetic field, which induces a current in the coils located in the latter. Often, the translator comprises a series of *SN* magnets with alternate polarities, whereas the stator hosts the copper coils. This mechanism, within the experimental setup, is simulated via a friction paddle with an adjustable normal force. The gravity field provides some part of the recentering force that is necessary to restrict the motion of the buoy. When, however, the wave exceeds a certain threshold, the translator is further restrained in its motion by an end-stop spring. This system also works as a booster for the translator's backup movement: the energy stored by compressing the spring is released when the cycle reverses, thus increasing the kinetic energy of the translator.

The data and the geometry considered in the following sections are presented in [25,42]. The tests at the Coastal Ocean and Sediment Transport (COAST) at Plymouth University (UK) were carried out with a cylinder float, which is identified by *CYL* in [25,42]; the characteristics of the geometry are given in Table 2. For the validation purposes within this research, reference is made to the extreme wave event *embedded focused waves*, which is also used in [25] for carrying out survivability analysis through numerical modeling of the Uppsala WEC. In particular, the data for the event defined by wave height $H = 7.20$ m (model scale $H = 0.36$ m) and wave period $T = 10.70$ s (model scale $T = 2.393$ s) is considered, for two different runs, in which the PTO friction damping is 5.00 kN and 59.00 kN, respectively (model scale

**Table 2**
Buoy dimensions of the Uppsala WEC.

| | Symbol | 1:20 model | Unit |
|---|---|---|---|
| Buoy radius | $R$ | 0.085 | m |
| Buoy draft | $D$ | 0.032 | m |

**Table 3**
Damping definition.

| Label | Full scale | 1:20 model | Unit |
|---|---|---|---|
| *C0* | 5000 | 0.63 | N |
| *C2* | 59 000 | 7.38 | N |

0.63 N and 7.38 N); the two cases are summarized in Table 3. These are chosen for being representative of two antithetical conditions: Case **C0** is the case where supposedly the harvesting function was deactivated — of course, some energy is damped out by the physical system that consists of pulleys and rails. Case **C2**, on the other hand, foresees the use of a breaking system that was activated by screws with a predefined, adjustable load, which adds a controlled damping value to the previous one. In this work, the different nature of the energy dissipation as described above is accounted for.

## 5. Numerical configuration

*General setting*

The numerical model is built upon the experimental setup reported in [42], herein using the 1:20th model scale thus making direct comparison to the available raw data.

The Uppsala WEC working principle combines a free-floating buoy with a linear magnet generator (PTO), which is attached on a ballasted platform and located at sea-floor level. The motion of the float is transmitted to the translator through a mooring line, making then the dynamics of the whole system quite complex and heavily dependent on the behavior of each part. Hence, the proposed model fully exploits the features made available by the two coupled libraries: Chrono and MoorDyn+. Several instances are combined to shape the system that can mimic the behavior of the PTO when connected to a float through a mooring line. In the following, a general overview of the numerical model geometry is given.

Using the schematic depicted in Fig. 1 as a template, Fig. 2 shows a mechanical model (left) and a 3D perspective view of the assembly (right) of the WEC, in which the different parts are labeled from *A*-*F*. Table 4 provides a synthetic description of the system regarding the elements and the libraries that handle their dynamics. Note that the only part interacting with fluid particles is the buoy ($A$). Although the elements from *B*–*F* are shown in the same 3D environment, they do not interact with water, much like the physical moving parts in the real case, which were installed aside the wave tank. Instead, accounting for the mooring line, in spite of the fact that such elements can interact with waves in a theoretical way, the line motion only depends on the fairlead and anchor positions, and the gravity acceleration. The line-to-water interaction is neglected here.

The solid surfaces of the float ($A$ in Fig. 2), where the most important part of the fluid–solid interaction takes place, consist of a set of boundary particles that are solved according to the mDBC algorithm that is presented in Section 2.4. The inertia of the buoy, which is not reported in the reference material, is computed by considering that the mass is uniformly distributed along the outer plastic shell, with a thickness defined in hindsight to comply with the total mass. It goes that the center of gravity of the buoy lies at the centroid location of the solid.

The mooring line is modeled here as a set of masses linearly joined by spring–damper items, following the approach presented in [69]. Element $B$ in Fig. 2 relates, in a non-linear fashion, the motion of the

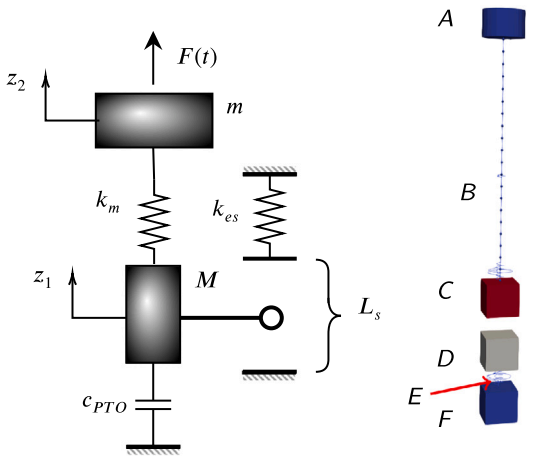


**Fig. 2.** Mechanical model of the PTO system with a moored buoy (left) and perspective visualization of the PTO assembly in the numerical model (right). The meaning of the symbols is given in Table 7, whereas the Latin letters from A–F are explained in Table 4.

**Table 4**
Instances and relative handler for the simulation of the Uppsala WEC.

| Label | Function | Instance | Manager |
|---|---|---|---|
| *A* | Buoy | Moving | Chrono |
| *B* | Taut line | Mooring line | MoorDyn+ |
| *C* | End-stop | Moving<br>Spring<br>Contact | Chrono<br>Chrono<br>Chrono SMC |
| *D* | Translator | Moving<br>Contact | Chrono<br>Chrono SMC |
| *E* | Energy | Damper | Chrono |
| *F* | End-stop | Contact | Chrono SMC |

buoy to the translator $D$. The line is initialized as a connection between the initial draft of the float and the bottom of the wave tank, which leads to an unstretched length $L_{us} = 2.468$ m. The stiffness of the line, which is given by the product of elasticity modulus and cross-sectional area ($EA_l$) is retrieved from the information given in [42]. [25] reports that an 8-meter-long polymer line (unstretched length $L_0 = 8.00$ m [25]) was used to connect the buoy to a mass that was supposed to mimic the translator; the line stretched 1% at a load of $F = 60$ N, thus giving:

$$K_{line.exp} = \frac{F}{0.010 L_0} = 750 \text{ N/m},$$

which represents the stiffness of the whole line, amounting to 6000 N of axial stiffness ($EA$). However, the numerical model only foresees one line that connects the buoy, at its draft, to the translator that virtually starts from the bottom of the flume. Here, to consider the same effects in terms of line stiffness, the line axial stiffness $EA_l$ is set to $L_{us} \cdot K_{line.exp} = 1830$ N.

Once the geometry of the line along its mechanical properties are defined, it is possible to proceed to assign the parameters to model the mooring line through the lumped-mass approach, according to the definitions given in Appendix B. Table 5 depicts the input values that are used to set up the line into the MoorDyn+ solver.

Note that the *Model time step* ($dt_M$) is defined according to the following relationship:

$$dt_M \leq \frac{10}{f_n}, \tag{11}$$

where $f_n$ identifies the critical frequency in the spring–mass system that describes the mooring line; its definition is given in Appendix B.5.

The PTO system that is employed in the Uppsala WEC functions as both harvesting device and safety system, having no clear definition

**Table 5**
Input parameters used for the definition of the mooring line.

| Element | Symbol | Quantity | Unit |
|---|---|---|---|
| Cross sectional stiffness | $EA_l$ | 1830 | N |
| Nominal diameter* | $D_N$ | 2 | mm |
| Spring constant | $k_m$ | 0.750 | kN/m |
| Segments | $N$ | 40 | – |
| Density in air* | $\rho_l$ | 1500 | kg/m$^3$ |
| Weight in fluid | $W_l$ | 0.015 | N |
| Natural frequency (Eq. (30)) | $f_n$ | 98.4 | kHz |
| Model time step | $dt_M$ | 7.0e−05 | s |

*The given values for these variable are plausible ones, not having any counterparts in the reference paper.

**Table 6**
Definition of the PTO generator damping models for the numerical simulations.

| Label | $F_\mu$ | $c_{PTO}$ |
|---|---|---|
| C0 | 0.000 N | 2.795 Ns/m |
| C2 | 6.755 N | 2.795 Ns/m |

of the two phases. Here, it comprises three solid objects, two moving ($C$ and $D$) and one fixed (F) (Fig. 2 and Table 4). The translator $D$ is bounded in its vertical motion by the upper and the lower end-stops $C$ and $F$, respectively, the former being movable and the latter fixed. The interaction between $D-C$ and $D-F$ is possible thanks to the contact tracing functionalities that are described in Appendix A.1. When the translator $D$ impacts the massless end-stop system $C$, its vertical motion is modified by the presence of a spring element, which exerts an elastic force according to the following relationship:

$$F_{Spring}(t) = k_{es} \cdot (l(t) - l_{es}) \tag{12}$$

where $l(t)$ is the spring length and $l_{es}$ is the equilibrium length of the *end-stop*.

The harvesting tool that is used in the physical tests is here represented by element $E$. For the aims of this work, as also stated before, the validation is performed considering two different setups for the generator (ref. Table 3). In particular, for case **C0**, described in [42] as the case in which no energy was harvested, a value that was representative of internal energy dissipation was utilized. To better represent this phenomenon, a velocity-proportional damping model is proposed. The damper element $E$ in fact obeys the following relationship:

$$F_{Damper} = c_{PTO}\dot{z} - \text{sign}(\dot{z})F_\mu, \tag{13}$$

where $c_{PTO}$ is the viscous damping coefficient, $F_\mu$ is the friction force given by the product of the friction coefficient and the transverse load. Table 6 reports the parameters that are used to reproduce the generator damping for Cases **C0** and **C2** in the SPH model starting from the values depicted in Section 3. Note that the Case **C0**, in spite of being defined as with *no damping*, needs to include some energy dissipation function in its definition to account for the internal resistance to the motion given by the various pieces of equipment that were used in the physical tests. For the aims of this research, the internal friction described above was modeled as velocity-proportional damping since it was found to be in better agreement with experimental evidence. The values reported in Table 6 are retrieved by using standard scaling procedures [70].

*PTO calibration*

Prior to validating the whole system, a first calibration of the proposed numerical model of the Uppsala WEC is performed against an analytical solution built upon the mechanical scheme shown in Fig. 2; this first phase takes place in a dry setting, as the fluid phase is completely absent. Since the goal of this section is the validation of contact tracing features and line behavior, only the **C0** case is used here, thus keeping its description more agile to be described through analytical models. The dynamics of the evolving system are assumed in

**Table 7**
Input parameters used for the analytical model.

| Element | Symbol | Quantity | Unit |
|---|---|---|---|
| Buoy mass | $m$ | 0.712 | kg |
| Line stiffness | $k_m$ | 0.750 | kN/m |
| End-stop stiffness | $k_{es}$ | 1.940 | kN/m |
| End-stop spring length | $l_{es}$ | 0.030 | m |
| Translator mass | $M$ | 0.780 | kg |
| Free Stroke | $L_s$ | 0.170 | m |
| Internal damping | $c_{PTO}$ | 2.625 | Ns/m |

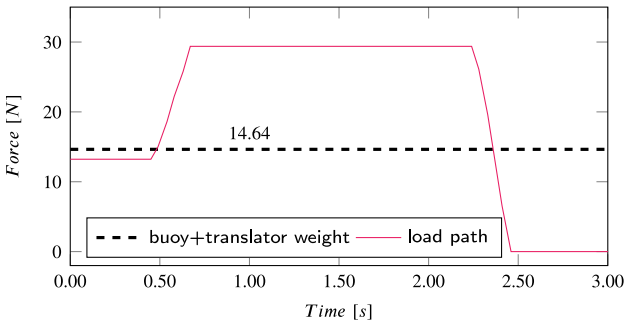


**Fig. 3.** Force time history used for the model calibration; the black dashed line reports the buoy and the translator weight.

the vertical direction only, and that the initial position of the translator is at its lowest ($-L_s/2$). The mooring line is simulated by a spring assuming that it will always be engaged in tension during this test. Note that this assumption will be satisfied by defining a particular external force time-history. The following equations describe the mechanical model:

$$\begin{cases} M\ddot{z_1} + c_{PTO}\dot{z_1} + K(z_1)(z_2 - z_1) = -Mg, \\ m\ddot{z_2} + k_m(z_1 - z_2) = mg + F(t), \end{cases} \tag{14}$$

where $M$ is the mass of the translator, $c_{PTO}$ is the applied damping, $g$ is the magnitude of the gravity acceleration, $m$ is the mass of the buoy, $k_m$ is the stiffness of the line, and $F(t)$ is the applied force; $z_1$ and $z_2$ are the position of the translator and the float, respectively. $K(z_1)$ represents the stiffness of the inner system and takes into account the presence of the end-stopping system. It can be defined by the following step function:

$$K = \begin{cases} k_m & \text{if } |z_1| < L_s/2; \\ k_m + k_{es} & \text{if } |z_1| \geq L_s/2; \end{cases} \tag{15}$$

where $k_{es}$ is the stiffness of the end-stop system.

The contact between the translator and the end-stop is handled only numerically and considering that there is a sudden variation in the stiffness of the system; a similar approach can be found in [25]. The time series of the driving force $F(t)$ is shown in Fig. 3: it is built to comply with the assumptions made beforehand. The initial 0.50 s of the time series report a constant force 10% lower than the weight of the system (that is, *Buoy mass+Translator mass*): this initial gap is necessary for the numerical model to reach an equilibrium position, where the line is taut and the translator at rest on the lower end-stop. The initial force in the line was found to be around 8 N.

Comparison of the numerical model response and the analytical solution is made in Fig. 4, where the solution of Eq. (14) is computed by integrating the system with a Runge–Kutta method fourth-order accurate. Three different simulations are performed with the numerical model, considering the effects of the initial inter-particle distance ($dp$) and the parameter $O_{contact}$ (overlap threshold) that assigns the accuracy of the external feature of the considered geometry for the contact tracing algorithm (inward and outward envelope). The overlapping threshold is defined in terms of $dp$. Despite being managed by the

**Table 8**
Parametric analysis for the model calibration.

| Label | $dp$ [m] | $O_{contact}$ $[dp]$ |
|---|---|---|
| ① | R/4 | 0.50 |
| ② | R/4 | 0.10 |
| ③ | R/5 | 0.10 |

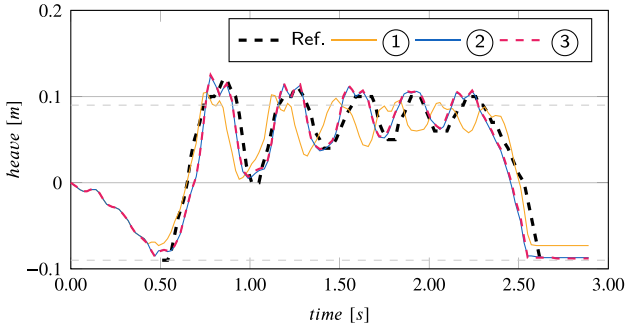


**Fig. 4.** PTO model calibration. The heave motion evolution of the model for the three cases collected in Table 8 are compared against the analytical predictions.

CHRONO SMC solver, the envelope shape offset is important for the accuracy of the collision detection: when the outer envelope shape far exceeds the actual geometry, a large gap can appear. On the other hand, envelope shapes too close can cause boundary penetration, which may cause *sticky* contact effects.

Table 8 reports the three cases that are used for the calibration of the parameters that matter for the contact tracing solver. Here, two initial resolutions are considered ($R/4$ and $R/5$), and two overlap threshold values. By comparing the evolution of the three cases with the reference solution, it can be concluded that the numerical model is able to reproduce the main characteristics of the PTO system, accounting for the role the elasticity of the mooring line plays along with its motion restriction. In such instances, however, the dynamics of the line is only considered in its linear range, which is an assumption that is violated when a real application is of interest. Nevertheless, this case serves well for the solely purpose of assessing the sensitivity of the model to the two parameters. It can be noticed that the parameter $O_{contact}$ is to be set meticulously. Case ① forms a large gap between the expected rest position – at $L_s/2$ – and the actual position of the translator. This is due to a repulsive effect generated by an excessive offset between the parent geometries of the translator and the end-stop, which as well results in a considerable difference in phase. Nevertheless, Case ② and Case ③ prove that the model can provide a reliable solution, not dependent on the initial inter-particle distance. A small gap is still appearing, which is considered to not affect the quality of the results, being the response of the system in phase with the target solution.

To conclude the calibration procedure, it can be observed that when the overlapping threshold $O_{contact}$ is small enough, the surface interaction is solved with accuracy and the system solution converges. For the following simulations, the parameter $O_{contact}$ is set to 0.10 $dp$. Furthermore, two simulations with $dp = R/6$ and $dp = R/7$, and $O_{contact} = 0.10\ dp$, were performed as well, providing the same accuracy as in the case with $dp = R/5$, and $O_{contact} = 0.10$; for the sake of readability of the chart, the time responses are not reported.

*Wave tank*

DualSPHysics allows deploying a set of built-in functions that are useful to design a suitable numerical tank that complies with the experimental conditions, without strictly reproducing the geometry. In fact, the tests in the COAST Laboratory were run in a wave basin of 35× 15.5 m, 2.5 m deep. A schematic of the numerical tank is presented in Fig. 5, in which the lateral and the top view are sketched. The tank has seen a dramatic reduction in length and width, but the depth complies with the experimental one to not alter the wave profile. The tank can be shortened thanks to using a piston-type wavemaker equipped with an active wave absorption system (AWAS) that guarantees the correct input incident wave, following the implementation proposed in [71]. The input motion at this position is generated from the incident wave gauged during the physical tests. The width of the tank is shrunk to three times the diameter of the floater, and to prevent lateral reflection, a numerical damping zone (shaded area in top view Fig. 5) that employs a quadratic decay function is applied in the $y$–direction [71]. Furthermore, to avoid any drag effects due to the presence of lateral solid walls, periodic boundary conditions are applied [72]. Downstream of the buoy there is an 1:3 anti-reflective beach which, boosted with numerical damping, provides a reflection coefficient lower than 3%.

## 6. Validation

### 6.1. Propagation of extreme waves

Purposing the model for the validation of the whole WEC, a first step is taken towards the validation of the wave tank in generating and propagating waves. This procedure is also common practice for assessing the accuracy of physical systems prior to running any tests. The extreme sea-state condition model that is employed to validate the SPH model is generated through a focused wave train which is constrained (embedded) into a regular wave background. The surface elevation of one such experimental test is reported in Fig. 6 (gray line), taken from [42]. The authors report that the test was carried out prior to including the float into the flume, and the wave elevation was measured at the buoy's location with a resistive wave gauge. In order to retrieve the wave characteristics to build the wavemaker motion, the signal is decomposed via a spectral analysis based on the Fourier Transform (FT) (via FFT). The regular body of the wave train, boxed in Fig. 6, has a wave period of $T_{reg} = 2.403$ s and a wave height of $H_{reg} = 0.27$ m whereas the focused part, as well boxed in the same figure, has $T_{focus} = 2.604$ s and $H_{focus} = 0.38$ m; both spectra are reported in Fig. 6. With these parameters for the regular wave train, joint with the 2.50-m water depth, it is possible to assert that the wave is traveling in intermediate water with a wave length of $L_{reg} = 8.50$ m, and that it can be ranked second order Stokes' wave. The phase between the regular background and the focused group is given as $\phi = \pi$.

The motion of the paddle is computed as follows. The regular wave body motion for 2nd order Stokes' waves is managed by an internal tool that is provided along with the software [71], which allows convenient use of an AWAS system to control over the quality of the generated waves. The unidirectional crest-focused wave is defined according to the *NewWave* theory [73]. The NewWave linear theory was firstly proposed by [74] defining the free-surface elevation $\eta(x,t)$ with respect to the sea-state power density spectrum $S_n(\omega)$, as linear superposition of $N$ wave modes. For a so-called crest-focused wave group, it goes:

$$\eta(x,t) = \sum_{n=0}^{N} a_n cos(k_n(x - x_f) - \omega_n(t - t_f)), \tag{16}$$

where $x_f$ and $t_f$ are the focusing position and focusing time, respectively. The amplitude of each component is given by:

$$a_n = \frac{A_{cr} S_n(\omega) \Delta\omega_n}{\sum_n S_n(\omega) \Delta\omega_n}, \tag{17}$$

where $\Delta\omega_n$ is the frequency increment, and $A_{cr} = \sqrt{2m_0 \ln(N)}$, where $m_0$ is the zeroth moment of the spectrum, is the linear crest amplitude. Note that the crest amplitude at $A_{cr}(x_f, t_f)$ equals the maximum wave height $H_{focus}$. Investigation carried out by [73] suggested that wave group generated by wavemakers that move according to the NewWave linear theory may lead to the introduction of spurious waves into the generated spectrum (see also [26]). To prevent this, the theory developed by [75] for second-order wave generation is used to correct the

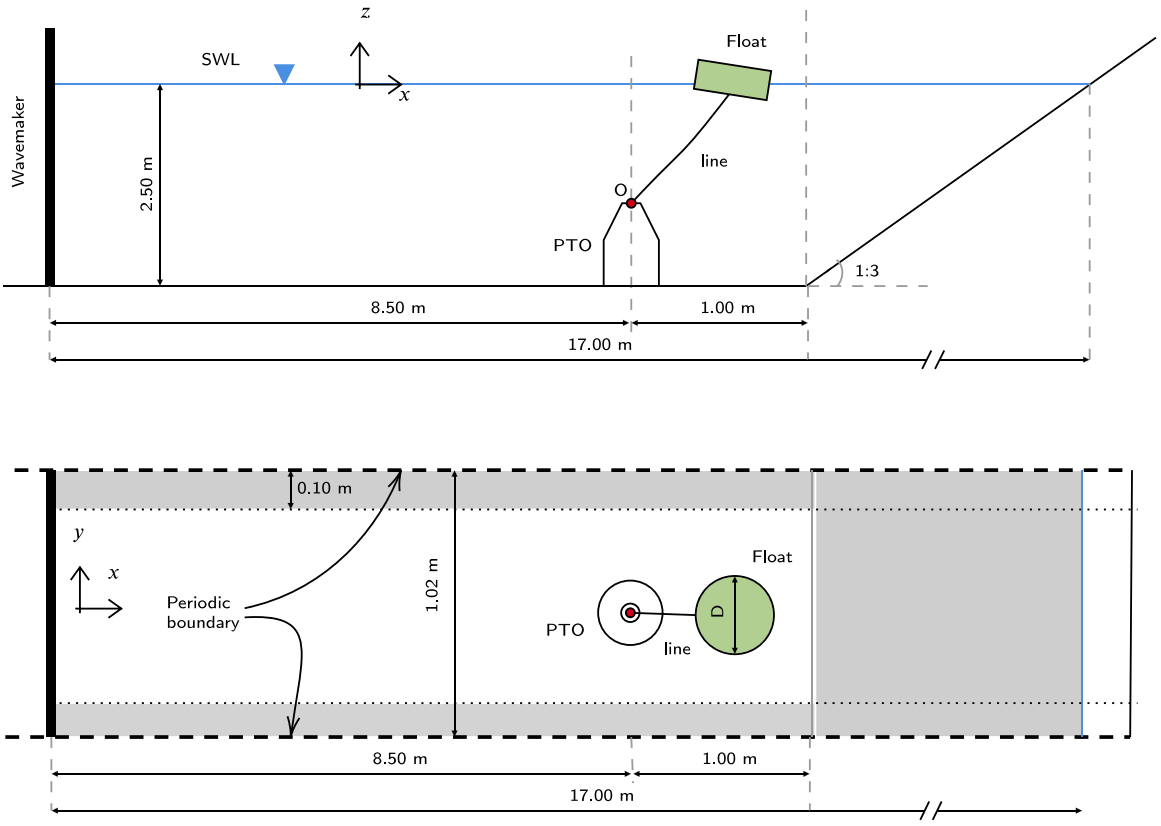


**Fig. 5.** Lateral and top views of the numerical tank for embedded focused wave tests. Following the experimental configuration, the point $O$ is actually located at $z = -2.50$ m: its representation is only for the sake of clarity.

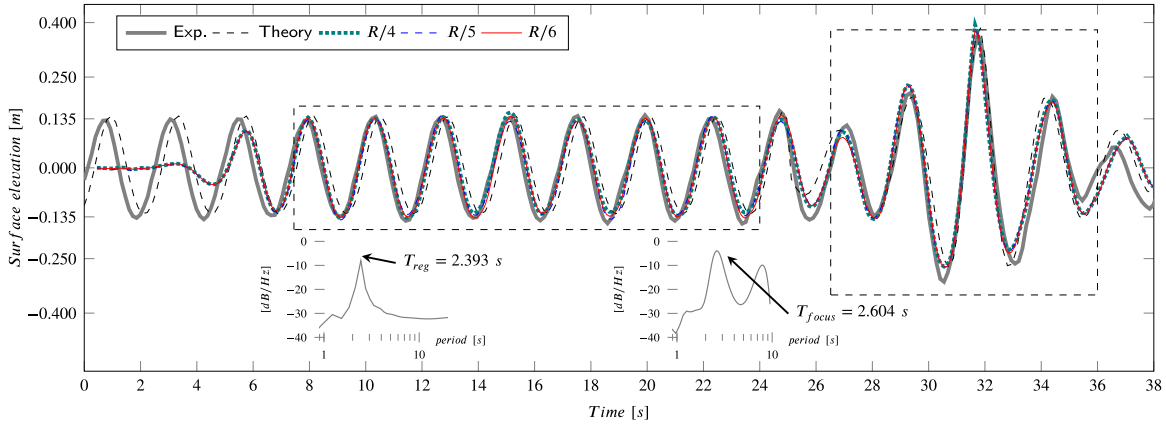


**Fig. 6.** Experimental, theoretical, and numerical surface elevations of the embedded focused wave. The two dashed boxes highlight the portion of the signal (Exp.) that is used to compute the spectra reported as insets.

motion input. Examples of focused waves simulation with DualSPHysics can be found in [26,76].

The paddle motion for the focused wave group is hence generated by considering $N = 1000$, which is also suggested in [73,77], and by generating a Joint North Sea Wave Observation Project (JONSWAP) [78] power density spectrum with a peak period $T_p = T_{focus}$ and a significant wave height $H_{m0} = 1.90 \cdot H_{reg}$. The wave group focuses at $x_f = 1L$, which corresponds to the initial position of the buoy, when the shortest wave in the spectrum reaches such position.

A standalone fluid validation is performed contrasting the obtained incident waves against the theoretical expectation for the surface elevation (Theory) and the physical data (Exp.), reported in Fig. 6. By visually comparing the experimental measurements to the expectation, it can be noticed that the latter does not fully comply with the former solely for some slight differences around *time* = 26 s, likely due to a misalignment where the two signals join. The outcome of the numerical model is reported in the same chart for three different particle resolutions, namely $R/4$, $R/5$, and $R/6$. Although it is customary to refer to the height of the wave for wave validations, the particle resolution is set based on the size of the float, thus preparing the model for future applications. The surface elevation evolution retraces with accuracy the target one with a few exceptions: around the point where two wave trains are spliced together, and around the two main troughs of the focusing group. At this stage it becomes important for the reader to keep this detail in mind because it can make the quality of the results below clearer.

Prior to moving to the full validation, a non-dimensional error estimator is defined to provide solid figures on the system accuracy. The

**Table 9**
Estimated errors for the wave tank in propagating extreme waves.

| $dp$ [m] | $W$ | $E_{T.reg}$ | $E_{T.focus}$ |
|---|---|---|---|
| $R/4$ | 0.843 | 1.8% | 2.2% |
| $R/5$ | 0.862 | 1.6% | 2.2% |
| $R/6$ | 0.877 | 1.6% | 2.1% |

index of agreement $W$, which was redefined by [79] over a previous definition given in [80]. It can account for amplitude differences and is of course sensitive to phase misalignment; $W$ for a specific signal $X_{num}$ with respect to a certain reference solution ($X_{exp}$) is estimated as follows:

$$W = 1 - \frac{\sum_{j=1}^{N_X}( |X_{num.j} - X_{exp.j}| )}{\sum_{j=1}^{N_X}( |X_{num.j} - \mu_{exp}| + |X_{exp.j} - \mu_{exp}| )} \tag{18}$$

where $N_X$ is the number of elements in the array $X_{num}$, and $\mu_{exp} = mean(X_{exp})$. The values provided by Eq. (18) are capped by +1 that indicates that the two signals are coincident. In this work, a scoring classification proposed in [81] for a similar index is used to rate the achieved accuracy. The proposed terminology, which pairs quantitative figures provided by Eq. (18) to qualitative descriptions; the classification defines as *excellent* for values of $W$ between 0.9 and 1.0, *very good* between 0.8 and 0.9, *good* between 0.7 and 0.8, *fair* or *reasonable* between 0.5 and 0.7, *poor* between 0.3 and 0.5, and *bad* lower than 0.3.

The quantifier in Eq. (18) is utilized to assess the accuracy of the model in generating and propagating constrained focused waves, and the results are reported in the second column of Table 9. The lengths of the compared time series comprise seven fully developed waves and the entire focused ground, as framed in Fig. 6 by the dashed rectangles and having the experimental data as reference solution. In addition, Table 9 depicts two extra columns that report error estimations in terms of period (and phase) for regular waves ($E_{T.reg}$) and for the focused group ($E_{T.focus}$). Overall, the tank presented in this section achieves a high degree of accuracy in reproducing the wave train, and it scores as *very good* according to [81]'s scale.

### 6.2. Validation of the full WEC

The validation procedure concludes by simulating the full physical setup numerically, using the test array depicted in Table 10; the two tests **C0** and **C2** are repeated three times considering different *dp*s. The results of these six simulations are presented in Figs. 7 and 8, respectively for the case with no applied damping **C0** and the case that mimics the energy harvesting phase **C2**. The investigated quantities are the heave and surge motion of the buoy, which are referred to its center of gravity, and the line force computed as the force at the fairlead connection to the translator mass. Before describing the results, it is important to remark that the *same* particle spacing is used to discretize the initial geometry of the solids. Additionally, Table 10 indicates the number of fluid particles per each simulation (fifth column) and the required runtime (sixth column) for solving the specified physical time (in parentheses) using the GPU accelerated version of the code.

The buoy motion (heave and surge, (a) and (b) in Figs. 7 and 8), respectively) shows overall good agreement in terms of period for both cases and for the three particle resolution, whereas the amplitude needs further discussion. Making reference to Fig. 7, the heave evolution matches perfectly with the experimental one, regardless of *dp*. On the other hand, the surge motion is consistently underestimated during the regular wave train; such a tendency is still in place while the focused train is hitting the float, but showing a slight horizontal average drift. A similar pattern can be observed in [44], where the same device is simulated, under the same wave conditions, with the meshbased fluid solver integrated in OpenFOAM; this work concluded that the surge underestimation was (excerpted from the [44]) "partly attributed to the fact that the [numerical] model neglects the line elasticity". In disagreement with this conclusion, the evidence produced by the proposed model shows that by neglecting the line stiffness it cannot fully explain the observed discrepancy. Moving on to Fig. 8, the heave motion initially follows the experimental trend; when, however, a form of steady state is reached, the heave is consistently overestimated for the regular wave train, whereas it fully agrees during the focused part. For what concerns the surge motion, the response shows similar features to the previous case.

**Table 10**
Case array for the WEC validation under embedded focused waves.

| Label | $F_\mu$ | $c_{PTO}$ | $dp$ [m] | Particles [$10^6$] | Runtime[a] |
|---|---|---|---|---|---|
| C0 | 0.000 N | 2.795 Ns/m | R/4 | 1.815 | 15 h (38.00 s) |
| | | | R/5 | 3.438 | 32 h (38.00 s) |
| | | | R/6 | 6.158 | 75 h (38.00 s) |
| C2 | 6.755 N | 2.795 Ns/m | R/4 | 1.815 | 13 h (33.20 s) |
| | | | R/5 | 3.438 | 30 h (33.20 s) |
| | | | R/6 | 6.158 | 64 h (33.20 s) |

[a]The values exposed in this column refer to simulations performed on a GPU NVidia RTX2080Ti.

**Table 11**
Estimated errors for the float motion (Heave and Surge) and the line force.

| Label | $dp$ [m] | $W$ Heave | $W$ Surge | $W$ line force |
|---|---|---|---|---|
| C0 | R/4 | 0.799 | 0.701 | 0.629 |
| | R/5 | 0.815 | 0.724 | 0.628 |
| | R/6 | 0.830 | 0.759 | 0.671 |
| C2 | R/4 | 0.631 | 0.712 | 0.640 |
| | R/5 | 0.659 | 0.725 | 0.656 |
| | R/6 | 0.658 | 0.709 | 0.717 |

The forces estimated in the line remain in agreement with the experimental references. For the case with no damping (Fig. 7(c)), the model provides an accurate response on account of both the time evolution and the overall magnitude of the peaks. During regular waves, the system shapes a pattern very close to the experimental trend, and the quality of the signal improves as the particle resolution does. In contrast with the motion of the buoy, the force evolution for the case with damping, **C2**, can be qualified as sufficiently accurate for the following aspects. First, the main peak is well caught, proving again that the particle resolution of the model can improve the quality of the results; however, the secondary peaks of the focused wave show a partial overestimation. Secondly, the regular part results in a different periodic pattern, which agrees with the reference data but for a spike in the aftermath of the wave crest.

A final picture of the numerical model performance is given in Table 11. The definition of $W$ (Eq. (18)) is run over the numerical time series reported in Figs. 7 and 8; the error is defined with reference to the experimental time series. For Case ***C*0** the model predicts quite well the heave motion, whereas the surge shows a consistent underestimation that makes it score as *good* (ref. [81]); the predicted time series for the line forces proves to be in *fair* agreement with the reference one. For Case ***C*2**, the model provides an overestimated time series for the heave motion, scoring as *reasonable*, whereas the surge motion and the line forces show similar figures as for ***C*0**.

Further insights about the performance of the Uppsala WEC can be inferred from the charts shown in Figs. 9 (translator and end-stop displacements, and line stretching) and 10 (translator velocity). The three charts report key information about the internal dynamics of the PTO system and the stretching function of the mooring line for the cases **C0** and **C2** with an initial particle spacing of $R/6$. The motion of the translator, which takes places along the $z$-direction, is mostly driven by the heave component of the buoy's motion due to the particular bound that the mooring line creates. A plausible figure for the work done by the surge component is around 2% of the overall work done by the

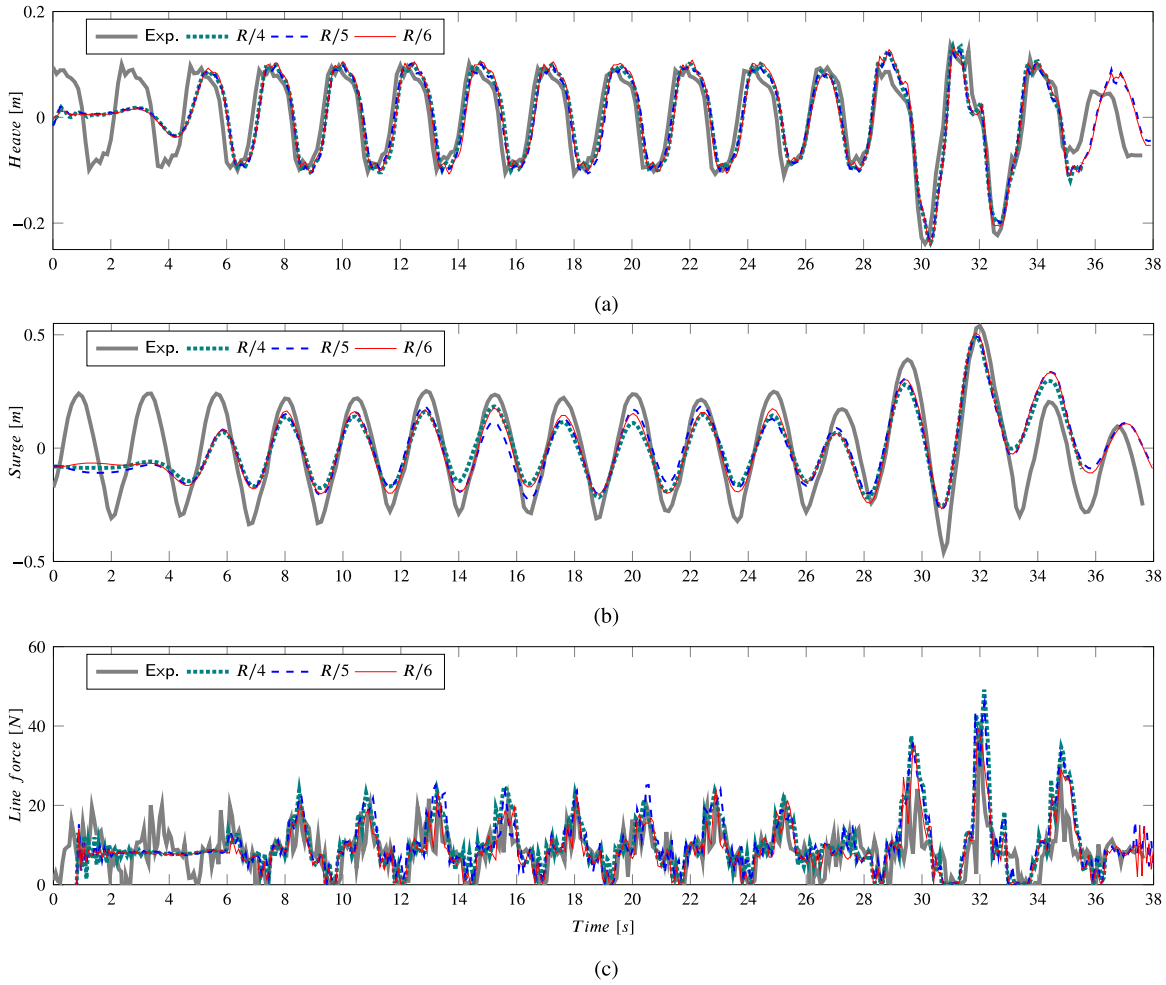


**Fig. 7.** Experimental and numerical buoy position in heave (a) and surge (b) motion, and line force (c) for the case with no PTO frictional damping (***C0***) reported in Table 8.

heave. The two charts 9(a) and 9(b) report the stretching evolution of the line that is computed as $L(t)-L0$, being $L(t)$ the length of the line in time. Note that in both panels, at the beginning of the simulations, the line stretches around 2 cm reaching equilibrium for a tension of around 9 N (refer to the first 3 s in 7(c) and 8(c)). For the case with no damping (Fig. 9(a)), the line stretches almost in unison with the motion of the translator, and some spikes appear when the translator hits the end-stop, which can be paired with the spikes shown in Fig. 10. On average, the magnitude of the stretch seldom exceeds the equilibrium value, due to the absence of resistance in the translator motion. On the other hand, the presence of a damping function in the PTO (Fig. 8(c)) strongly changes the stretching function: the line is engaged with higher tension for the moment the translator starts its motion, showing fainter peaks at the moments of impact.

Fig. 11 reports six frames of the simulation **C0** when the main peak of the focused train is striking the buoy; the first row depicts the velocity field interpolating values over the particles surrounding the float, and the second shows the $y$-component of the vorticity field over the computational nodes. Three instants of the simulation are captured here, namely when the main crest of the focused wave approaches the float (a) and (d); the crest is at buoy's location (b) and (e); and immediately after the crest overtakes the float (c) and (f), in the moment when the line force peaks. In addition, the frames point out the non-breaking nature of the waves described by the numerical model, which reduces the likelihood of slamming loads onto the float outer surface (for more see: [28]). The vorticity field shows the effects of the interaction of the body with the surrounding fluid, highlighting a high mass transport around the hull of the device. As a whole, the device is utterly submerged during this event, thus hampering the presence of slamming loads.

By discussing the quantities not reported in the experimental pool of data, useful information can be deduced. First of all, the presence of a damping function helps in reducing the magnitude of the forces that are generally experienced on the internal components of the power take-off and on the mooring line, thanks to the smoothing effect of the magnetic field on the dynamics of the translator. The line sees a more stable stretching function, which, in turn, implies a force trend more suitable for investigating fatigue cycles. However, the peak force is hardly altered by the presence of the damper, due to similar peak speeds at the moment of impact of the end-stop during the main peak of the focused wave. Finally, it can be concluded that higher snatching forces are expected when the line retakes tension, due to the combination of the inertia of the translator and the frictional force of the damping system.

Trying to hypothesize the reasons for the mismatching in some of the previously exposed quantities, it is possible to highlight some of differences in the physical and numerical configurations, the most important of which is the mass distribution on the geometry of the float. This conclusion is strengthened by the agreement shown in Fig. 8(a) when the motion is driven by the focused wave group: in this circumstance, the pitching motion becomes negligible due to the type of forces involved and only the shape of buoy can affect the magnitude of the force. Another source of discrepancy may arise from the wave-line interaction which can affect the magnitude of the force, albeit neglected in this work. It is worth mentioning that the artificial viscosity treatment used for this validation may have played a meaningful role in the

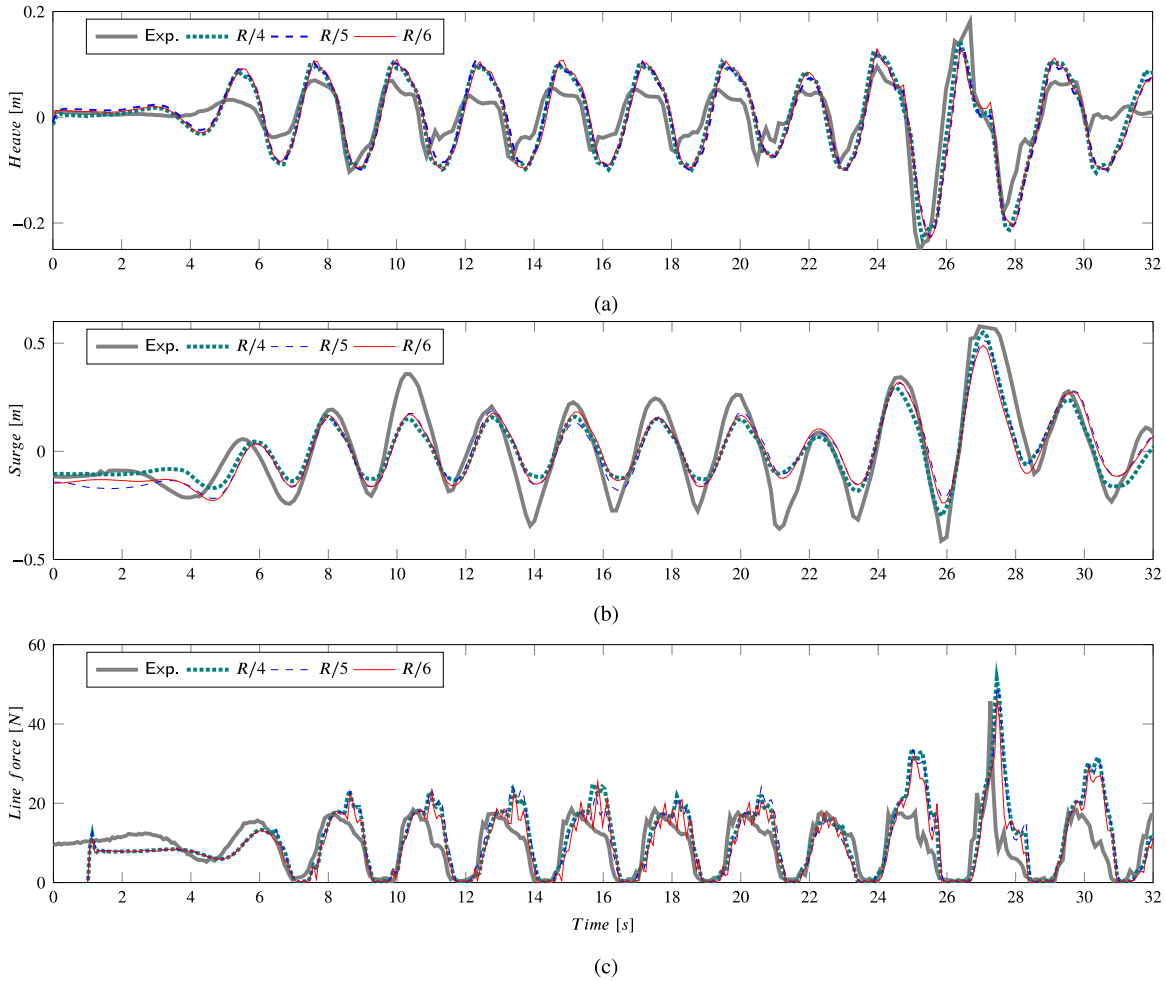


**Fig. 8.** Experimental and numerical buoy position in heave (a) and surge (b) motion, and line force (c) for the case with PTO frictional damping (***C2***) reported in Table 8.

phenomenon under discussion. However, further research is needed to identify the nature of this numerical–experimental mismatching, which occurred for the simulations presented in this work and it was observed in [44] as well.

## 7. Study with irregular waves

Extreme loads are typically defined as the maximum loads that can be expected during a specific duration, e.g., the n-year design loads. The return period must be defined according to the nominal life of the structure and to the expected failure mode [21]. As such, for the aim of the following analyses, the considered wave condition is not indicative of any specific safety check (more on this in EN1998 [21]); instead, it is used as a proxy for showing the general capabilities of the proposed tool. As a matter of fact, also specified in the reference research [25,42], the chosen event corresponds to a return period of 80 years at the Wave Hub site, located in southwest UK. This event was not chosen for a specific purpose, being not linked to any specific safety check thereafter performed (i.e., the Limit State was not identified).

The study performed in this section determines the dynamic response of the Uppsala WEC under irregular sea states, representative of realistic, extreme conditions. The time series of irregular waves is generated using a JONSWAP power density spectrum by means of an internal tool [82]. A stretched algorithm as described in [71] is used to define the band-width of the irregular wave train that has significant wave height $H_{m0}$ = 0.27 m and peak period $T_p$ = 2.393 s in 2.50-m water depth. To obtain a series of 500 waves, 1200 s of physical time are used to run the simulation; hence, the computational time is balanced by performing the following analyses (with and without device) discretizing the domain with an initial inter-particle distance $R/5$ (ref. Table 10), resulting in a computational time of roughly 800 h (30 days). This initial particle spacing provides sufficient accuracy as shown Table 11.

The same configuration of the numerical tank presented and validated in Section 5 (Wave tank) is utilized for wave generation and propagation. The motion of the piston is internally computed to match the time series, and corrected in time by an AWAS system. The accuracy of the system's generation and propagation capabilities is assessed through a simulation devoid of the device; the wave surface elevation at the buoy's location is gauged and analyzed by means of an FTT. Fig. 12 depicts the reference wave density spectrum, the theoretical one, and the numerical one. This comparison shows that the system produces the target free-surface elevation with sufficient accuracy, capturing the peak period with a 3%-error and slightly overshooting the $H_{m0}$ value of about 4%.

The whole numerical domain validated in Section 6 is used to express the extreme forces as function of the PTO configuration. According to the values of the applied damping shown in [42], four test cases (**I0-I3**) are defined to evaluate the response of the system under irregular waves. The configuration of the damper for each case is presented in Table 12. To better adhere real PTO system working principles, the Coulomb-like damping is no longer included here, thus using solely a velocity-proportional one. The parameter $c_h$ is deemed to be representative of the energy conversion process that takes place into the PTO (adjustable), whereas $c_{PTO}$ simulates the internal dissipative

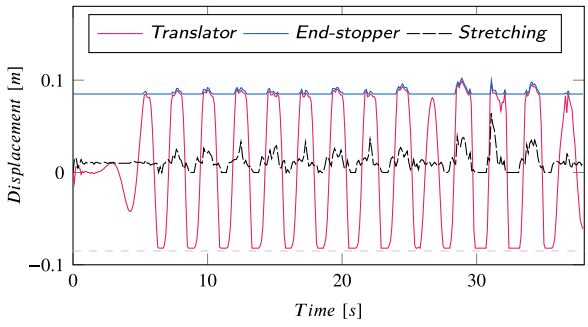


(a)

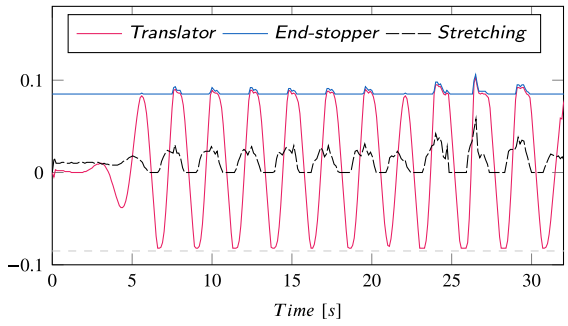


(b)

**Fig. 9.** Translator and end-stop displacements evolution, and line stretching function during case **C0** (a) and **C2** (b) reported in Table 8, for the initial particle spacing $R/6$. The dashed gray lines report the lower bound of the end-stopping system, which is fixed.

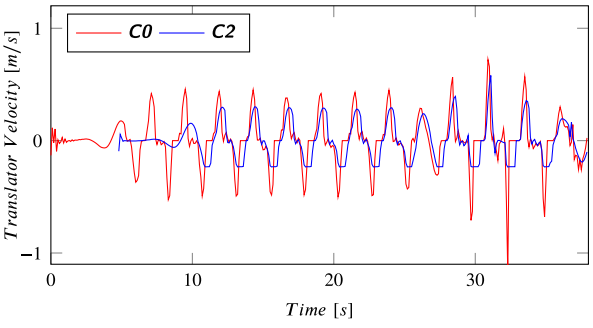


(a)

**Fig. 10.** Translator velocity evolution during case **C0** and **C2** reported in Table 8, for the initial particle spacing $R/6$.

**Table 12**
Definition of the generator damping for the numerical model analysis under irregular waves.

| Label | $c_h$ | $c_{PTO}$ |
|---|---|---|
| I0 | 0.000 Ns/m | 2.795 Ns/m |
| I1 | 3.333 Ns/m | 2.795 Ns/m |
| I2 | 6.755 Ns/m | 2.795 Ns/m |
| I3 | 9.725 Ns/m | 2.795 Ns/m |

mechanisms, shared among all the cases (fixed). Note that the Coulomb-to-viscous transformation is performed according to the scale factors given in [70].

The output of the numerical model for the four configurations presented in Table 12 is post-processed according to the following query. The wave height evolution measured in front of the device in each test is partitioned into single periods $T_i$ with a down-zero-crossing function; the zero-cross procedure has been set to include in each time window a trough and the ensuing crest. In agreement with the identification of each zero-cross interval, the other quantities are partitioned as well. Specifically, within each $T_i$, the wave height $A_i$ is calculated as the straight sum of the minimum and maximum absolute values of the free-surface elevation function; mins and maxs are then also combined to define another quantity, $H_i^2 = H_{max.i}^2 + H_{min.i}^2$ that may be considered as representative of the wave energy content; using the available information of the translator motion, the PTO absorbed power per period $P_i = c_h \int \dot{z}^2 dt$ is built; finally, the velocity evolution of the translator is used to retrieve the peak velocity per period $V_i = max(|\dot{z}|)$. Furthermore, the line force in each $T_i$ is taken as the force peak within the identified time window, that is, $F_i = max(F_{line})$.

The charts proposed in Figs. 13(a) and 13(b) make use of the subsets of data computed in the preceding step. The former employs the wave height $A_i$ and the peak force $F_i$, and it shows a scatter plot for each duo of wave height-peak force for the two extreme cases ***I0*** and ***I3*** in terms of damping. The second chart proposes an extreme value analysis of the peak force $F_i$ through the exceedance probability function for the line forces of the four irregular wave tests ***I0*** − ***I3***. The main body of forces is linearly correlated to the wave height, clearly identifying a threshold where the slope of the relationship dramatically increases. This point (around $A_i \approx 0.27$ m) corresponds to the activation of the end-stopping system. Being the threshold higher than the total stroke due to the fact that the mean period of the hitting waves is not nearly close to the fundamental heave period of the system, which refers to the structure without end-stopping system. As pointed out by previous research on the same device [25,42,44], the main effect of increasing the PTO is to mild the extreme actions on to the system, which is consistently reported in this research as well. By comparing the trend of each data set (dashed lines in Fig. 13(a)), this aforementioned result is more visible. This is also straightened by the pattern of the lines reported in Fig. 13(b), which substantially show that the configuration with no damping is more likely to experience higher forces.

The data used in the extreme value analysis (Fig. 13) can provide an estimate of the maximum loads that might be expected to occur for the specified return periods. It is clear that the system benefits from the increase in internal damping for what accounts extreme values, for example, of the line forces. As a drawback, however, the damping shifts the force plateaus around smaller wave amplitudes — this fact concerns the most when fatigue analysis of the system is performed. A thorough design of the line diameter, material, and kind of fairlead connections should account for both conditions, as such fulfilling all the design requirements at once. A final piece of insight can be gained from inspecting the dependence of the exceedance probability on the PTO damping: it suggests that a value in between the cases **I1** and **I2** could provide the right balance between the serviceability and the survivability safety checks (safety and function).

Complementary to the previous analyses, a final part of this investigation deals with an in-depth examination of the dataset presented at the beginning of this section. For the four cases **I0-I3**, Fig. 14 charts the measured line peak forces against the individual wave height of the incident wave $A_i$ (first column); the sum of the squared crest and trough $H_i^2$ (second column); the PTO absorbed power per period $P_i = c_{PTO} \int \dot{z}^2 dt$ (third column); and the maximum translator velocity per period $V_i = max(|\dot{z}|)$ (fourth column). Each scatter plot is fitted by a least-squares line and includes the Pearson correlation coefficient $\rho = \rho(F, Q)$, where $F$ arrays the $F_i$ scalars, and $Q$ arrays the four variables (i.e., $A_i$, $H_i^2$, $P_i$, and $V_i$).

Fig. 14 suggests that the damping increases the linearity of the system's response, considered in terms of forces, for the four defined quantities. The first two rows show a high dispersion of the scatter plots as well around the fitting lines, whereas rows three and four show a more stable behavior and both the wave height and the wave energy could be used to make predictions about the evolution of the system for

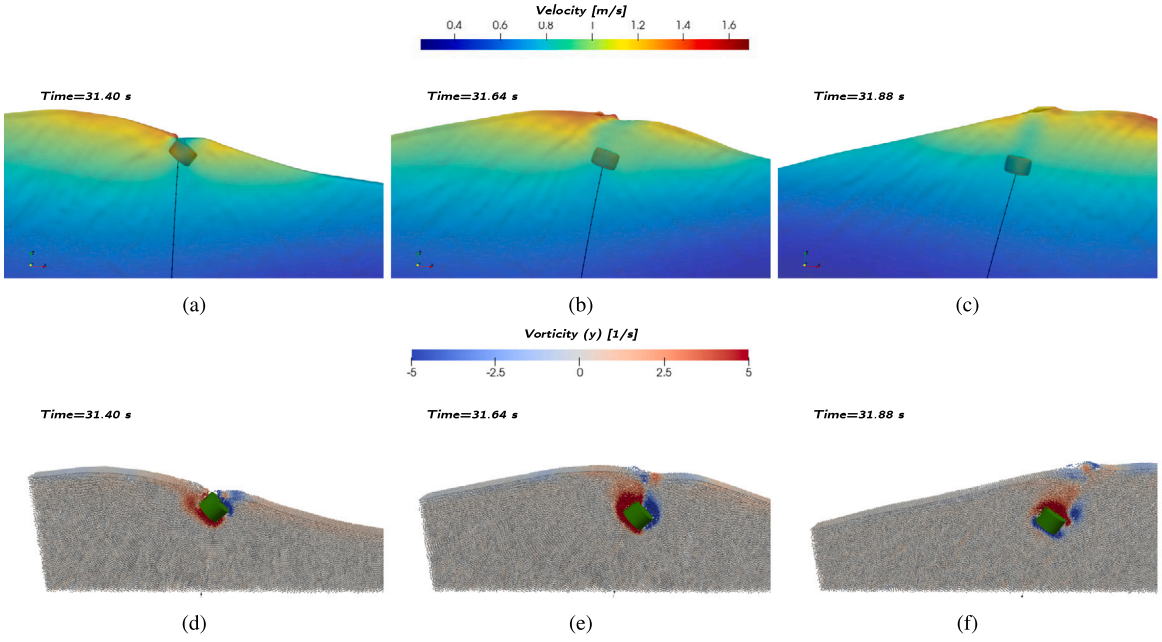


**Fig. 11.** 3D visualization of the numerical simulation **C0** for the resolution $R/6$. The snapshots represent three instants of it, respectively: the main crest of the focused wave approaching the float (a) and (d); when the crest is at buoy's location (b) and (e); and just after the crest (c) and (f), when the line force peaks. The colorbar above each row of frames reports the velocity magnitude for the surfaces, and the vorticity for the particle array around the float.

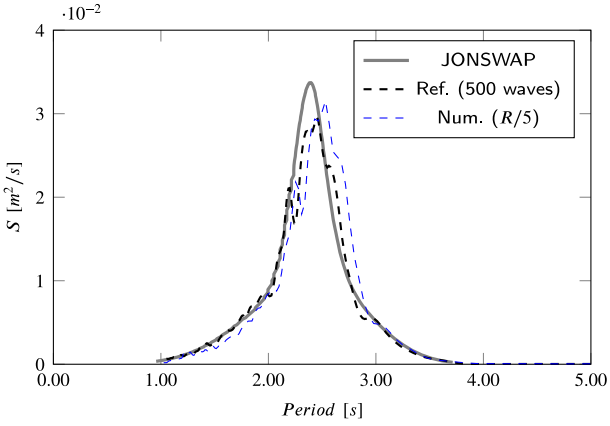


**Fig. 12.** Wave spectra for the case of irregular waves, comparison between the JONSWAP spectrum ($T_p$ = 2.393 s, $H_{m0}$ = 0.27 m, depth= 2.50 m), the reference one obtained with 500 wave periods, and the numerical one (resolution $R/5$) obtained from a simulation without the device.

modified conditions. The first two columns, which could be seen as a re-arrangement of the data in Fig. 13, prove that when a relevant value of the PTO damping is included in the system, its response correlates well with the external cause. The fourth column, instead, reveals that the peak velocity of the translator sensibly reduces with the increase of damping, meaning that the nature of the peak force is not related to translator hitting the end-stop, which can be taken as the instant when the velocity peaks, but rather to the end-stop spring reaching its maximum compression.

The following conclusions can be drawn from the extreme analysis presented in this section. The Uppsala WEC surely benefits from utilizing a greater value for the PTO damping: in the first place, more power is harvested by the system for smaller wave amplitudes and this may increase its revenue assuming that the system is connected to the grid; secondly, the reduced mobility of the translator inside the PTO can diminish detrimental effects on to the casing and, in turn, on the foundation. However, this effect is relegated to certain

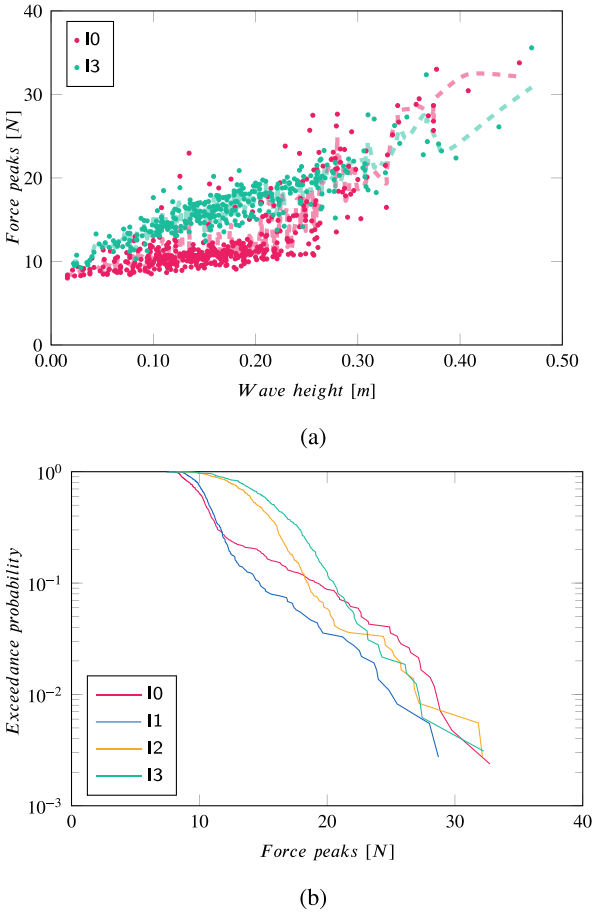


**Fig. 13.** (a) Measured force peaks for the four irregular wave tests ***I0*** and ***I3***, plotted against the individual wave height of the numerical incident wave. The dashed lines represent the running average of each set of data and are included to improve the chart readability. (b) Extreme value analysis through the exceedance probability function for the line forces of the four irregular wave tests ***I0*** – ***I3***.

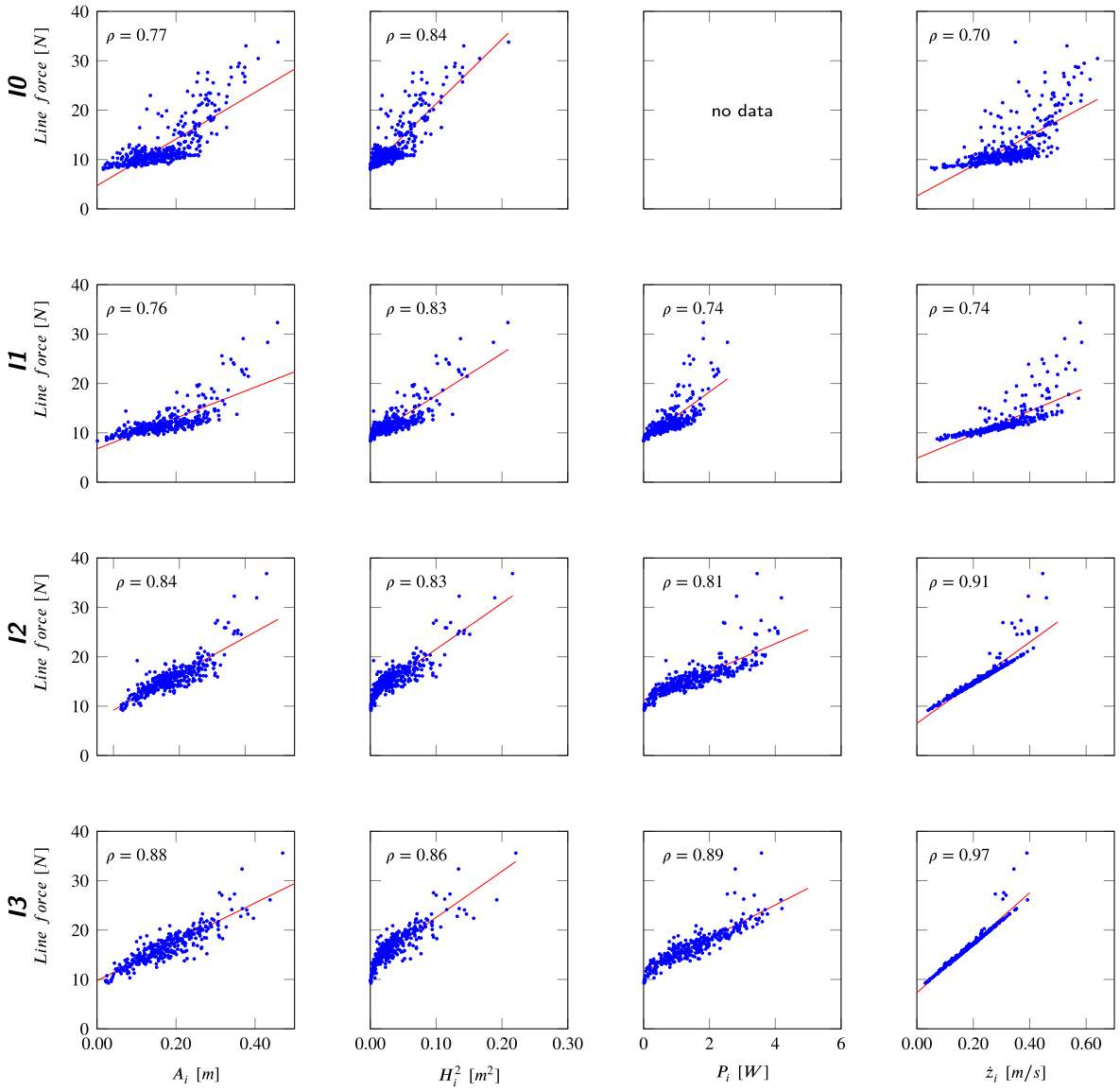


**Fig. 14.** Measured force peaks in irregular wave test $I0-I3$ plotted against the individual wave height of the incident wave $A_i$ (first column); the squared individual wave height $H_i^2$ (second column); the PTO absorbed power per period $c_h \int \dot{z}^2 dt$ (third column); and the maximum translator velocity per period $\dot{z}$ (fourth column). Each scatter plot reports the value of the Pearson correlation coefficient $\rho$ and a least-squares (red) line.

values of damping and only for extreme forces. It turns out that the harvesting function performance and the lifespan of the mooring system are interlocked. The optimization of the system must account for this feature, balancing the expected line load in the various conditions.

The end-stopping system could also see improvement. Its spring represents a booster during energy harvesting, but the primary duty of this element is to protect the system against extreme events. Hence, a way to reduce the peaks of the force would be to reduce the stiffness of the spring, which entails a longer spring length and with cascading effects on the design of the structure as a whole; it could also include a viscous damper, thus making it more similar to a shock-absorber.

## 8. Conclusions

Using the Uppsala WEC as a benchmark, this work has validated an open-source piece of software that combines the functionality of two different computing libraries. The time evolution of the incident wave, of the heave and surge motion, and the line force for two different PTO configurations are validated with contrasting experimental data. It showed that the mesh-less nature of the Smoothed Particle Hydrodynamics method has the right degree of maturity in handling survivability simulations of floating devices meant for wave energy conversion. Compared to meshbased solvers, violent and sudden changes in device configuration and fluid mechanics do not affect the stability and convergence of the system. Overall, DualSPHysics represents a useful asset for studying the kinematics of marine structures, and it can complement the set of tools already available for investigating wave energy converters.

The dataset presented in this research paper demonstrates that the proposed numerical model can capture the experimental behavior of the Uppsala WEC point absorber with sufficient accuracy, envisaging its use for analyses beyond this initial configuration. The proposed numerical method has shown to be apt for the simulation of real wave energy converters under extreme conditions. The validation was performed using the Uppsala WEC, which is composed of a float, a mooring line, and a complete power take-off system located at the sea floor, which includes end-stopping systems. The calibration and validation procedure could also be used to model devices with features similar to those of the Uppsala WEC, where the complex interaction of mooring

lines, mechanical constraints, and, of course, fluids themselves cannot be disregarded, rather must be included to get reliable information.

This work suggests that the Uppsala WEC performance can be improved. The management of the PTO internal damping turns out to be critical to enhancing the capability of the device, for short- and long-term conditions, and could be used to increase the robustness and resilience of the system. In fact, a system with self-adjustable internal damping, variable in time and in accordance with prior knowledge of the sea state actually impacting the device, may increase the device's life expectancy. The end-stopping system could see improvement as well. Although during the simulations carried out for this research the free stroke never exceeded the maximum allowable stroke, spring stiffness may be downgraded and coupled with a damper; this may reduce the harvesting capabilities of the system, but it will surely reduce the overall maximum actions.

Computational costs notwithstanding, a high-fidelity model, such as the one presented in this paper, can be used to run long simulations, considering complete sea states, and considering the high efficiency of the DualSPHysics framework, it is doable even without using HPC systems. Indeed, the expense of CFD simulations is well balanced by the accuracy that they can provide. The execution of these tests numerically leads to further knowledge of the system response with a high degree of detail, while the reproduction of the PTO system with a highly non-linear response, closely resembling real ones, allows investigating the response of the system in energetic sea-state conditions. This can provide feedback on possible strategies to be used to avoid oversizing while maintaining comparable degrees of reliability.

The applicability of numerical models to solving engineering problems is now beyond question. However, the convergence and stability problems that can arise when using state-of-the-art tools are not the only obstacles to using them to simulate wave energy converters. Passive and active control systems are a common practice for improving power capture performance; numerical simulations of dedicated hardware and software require a further improvement of the proposed code. On the validity and reliability of the results obtainable from the proposed model, it can be stated that the scale of the device that was used for validation purposes is relatively high, so much so that it can be expected that they have comparable effects from the fluid viscous forces (see [83]). Additional challenges arise from the way the power take-off is simulated. For example, when scaling the results to full, the pulley system used in the experiments has no full-scale analogs in the offshore environment and the mooring line elastic properties are generally different, although it may be selected to be consistent with the dynamic properties of real counterparts (see [84]). However, more research is needed to improve the reliability of scaling procedures for point-absorbing wave energy converters.

## CRediT authorship contribution statement

**Bonaventura Tagliafierro:** Conceptualization, Validation, Investigation, Methodology, Formal analysis, Data curation, Visualization, Writing – original draft. **Iván Martínez-Estévez:** Software, Resources, Writing – review & editing. **José M. Domínguez:** Software, Resources, Writing – review & editing. **Alejandro J.C. Crespo:** Conceptualization, Validation, Visualization, Methodology, Formal analysis, Data curation, Investigation, Writing – original draft, Supervision, Resources, Funding acquisition. **Malin Göteman:** Investigation, Validation, Data curation, Writing – review & editing. **Jens Engström:** Investigation, Validation, Data curation, Writing – review & editing. **Moncho Gómez-Gesteira:** Methodology, Visualization, Supervision, Writing – review & editing, Project administration, Resources, Funding acquisition.

## Declaration of competing interest

The authors declare that they have no known competing financial interests or personal relationships that could have appeared to influence the work reported in this paper.

## Acknowledgments

Funding for open access charge: Universidade de Vigo/CISUG, Spain. This work was supported by the project SURVIWEC PID2020-113245RB-I00 financed by MCIN/ AEI /10.13039/ 501100011033 and by the project ED431C 2021/44 "Programa de Consolidación e Estructuración de Unidades de Investigación Competitivas" financed by Xunta de Galicia, Consellería de Cultura, Educación e Universidade, Spaon. This work was also partially supported by COST Action CA17105 WECANet "A pan-European Network for Marine Renewable Energy with a Focus on Wave Energy", supported by COST (European Cooperation in Science and Technology) which is funded by the Horizon 2020 Framework Programme of the European Union. COST is a funding agency for research and innovation networks.

B. Tagliafierro acknowledges funding from Italian Ministry for Education, University and Research (MIUR) as part of the program "Dottorati Innovativi a caratterizzazione industriale" (ID DOT 1328490-3), funded by the European Union (Structural Funding ERDF-ESF for "Research and Innovation" 2014–2020). I. Martínez-Estévez acknowledges funding from Xunta de Galicia, Spain under "Programa de axudas á etapa predoutoral da Consellería de Cultura, Educación e Universidades da Xunta de Galicia" (ED481A-2021/337). M. Göteman and J. Engström acknowledge funding from the Centre of Natural Hazards and Disaster Science, Sweden, STandUP for Energy and the Swedish Energy Authority (project number 47264-1). The authors wishes to express their gratitude to the IT team's support (EPhysLab, University of Vigo) in using the HPC system at http://monkey-island.uvigo.es. The authors are grateful to Dr. Corrado Altomare (Polytechnic University of Catalonia) for his insightful comments.

## Appendix A. Coupling with project Chrono

### A.1. Collision algorithm: smooth-contact code

Nonfluid objects are schematized as a set of particles; their motion is imposed by the system of Eqs. (9)–(10), being the cause defined in (7). When the distance between two approaching particles of two different floating objects is within the interaction radius, another branch of the code is demanded to estimate the forces that develop at contact. For the application presented in this study, the soft-sphere discrete element method (DEM) implemented in the Project Chrono library is employed; this approach considers the outer envelope surface of bodies to be deformable, which entails that the surfaces can overlap during their collision to a certain extent. Following the Project Chrono library coupling, the smooth-contact code (SMC) available from version Chrono-4.0.0 with a single-core module (DEM penalty-based in [33]).

Due to the particular motion imposed to the colliding rigid bodies, in the following, a description of the contact force that develops in the normal direction of collision is given. In fact, tangential forces are negligible and restricted to second-order deformations due to the motion of the PTO system being modeled in this work. The colliding objects (translator and the two end-stoppers (ref. to Fig. 2)) are restricted to move along the same axis.

The normal contact force $\boldsymbol{F}_n$, according to the model presented by [85]:

$$\boldsymbol{F}_n = k_n \delta_n^{\frac{3}{2}} \hat{\boldsymbol{n}} - c_n \delta_n^{\frac{3}{2}} v_n, \tag{19}$$

where $k_n$ is the normal stiffness, $c_n$ is the normal damping, $v_n$ is the normal component of the relative velocity at the point of contact, $\delta_n$ is the normal overlap, and $\hat{\boldsymbol{n}}$ is the unit vector pointing from one particle center to the other. The quantities $k_n$ and $c_n$ are defined automatically by the Chrono module starting from the user-defined modulus of elasticity $E_v$, Poisson's ratio $\nu_c$ and coefficient of restitution $e$. More details are given in [86].

The extent of overlap, relative collision velocity, and other material properties are used to calculate the forces and torques acting on the bodies. Then, particle positions and velocities are updated by resolving all forces and torques in the N-body system (Eqs. (8) and (9)).

### A.2. Mechanical restrictions: spring damper

The translational degrees of freedom between rigid instances can include reactive forces according to their relative motion. The element that is able to exert this force is called *spring–damper* element. Let $i$ and $j$ be two points belonging to two bodies, respectively; the relative force can be defined such that:

$$F_{sd} = c_{sd}\boldsymbol{v}_{ij} \cdot \hat{\boldsymbol{t}}_{sd} + k_{sp}\boldsymbol{r}_{ij} \cdot \hat{\boldsymbol{t}}_{sd} - f_{sd}\hat{\boldsymbol{t}}_{sd}, \tag{20}$$

where $c_{sd}$, $k_{sd}$, and $f_{sd}$ are the viscous damping coefficient, stiffness, and friction damping that are implemented in the element, respectively; $\boldsymbol{r}_{ij}$ and $\boldsymbol{v}_{ij}$ are the relative position and velocity between points $i$ and $j$. The term

$$\hat{\boldsymbol{t}}_{sd} = \frac{\boldsymbol{r}_j - \boldsymbol{r}_i}{|\boldsymbol{r}_j - \boldsymbol{r}_i|}, \tag{21}$$

is the direction along which the force is applied; $\boldsymbol{r}_i$ and $\boldsymbol{r}_j$ identify the position of the points. Note that no predictive algorithm is used for the final position of the connected nodes, thus the force is identified at each time step within one loop.

## Appendix B. Coupling with MoorDyn+

### B.1. Lumped-mass mooring line model

The lumped-mass approach consists in partitioning the entire *unstretched* length of a line ($L_0$) into $N$ equally long segments, generating an $N + 1$ number of nodes. The position of each node that makes up the line in an absolute reference system is stored as $\boldsymbol{r}_i$, with $i$ spanning over $i = 1...N + 1$. The properties of each segment are inherited from the overall geometry of the line, which is defined by the parameters: $l = L_0/N$; volume-equivalent area ($A = \pi/4d^2$, being $d$ the volume-equivalent diameter), density($\rho$), net mass $m_i = Al(\rho - \rho_w)$, being $\rho_w$ the water density), elasticity modulus ($E$), and internal damping coefficient ($C_{int}$). An important assumption is made on the kinematics of the node: the tangential direction is defined as:

$$\hat{\boldsymbol{t}}_i = \frac{\boldsymbol{r}_{i^+} - \boldsymbol{r}_{i^-}}{|\boldsymbol{r}_{i^+} - \boldsymbol{r}_{i^-}|}, \tag{22}$$

where $\boldsymbol{r}_{i^+}$ and $\boldsymbol{r}_{i^-}$ identify the position of the proceeding and the following nodes in the line, respectively. It must be noticed that this procedure cannot be applied to the boundary nodes.

### B.2. Internal forces

The system of equations that is ultimately solved to identify the position of each node is built by considering the internal forces coming from the two connected segments. Based on the hypothesis that each segment behaves as a spring–damper element, the internal forces net buoyancy $W$, can be defined as follows.

$$\boldsymbol{W}_{i^+} = m_i * \boldsymbol{g}, \tag{23}$$

$$\boldsymbol{T}_{i^+} = EA\epsilon_{i^+}\frac{\boldsymbol{r}_{i^+} - \boldsymbol{r}_i}{|\boldsymbol{r}_{i^+} - \boldsymbol{r}_i|} \cup \epsilon_{i^+} > 0, \tag{24}$$

$$\boldsymbol{C}_{i^+} = C_{int}A\dot{\epsilon}_{i^+}\frac{\boldsymbol{r}_{i^+} - \boldsymbol{r}_i}{|\boldsymbol{r}_{i^+} - \boldsymbol{r}_i|} \cup \epsilon_{i^+} > 0, \tag{25}$$

where $\boldsymbol{g}$ is the vector of gravity acceleration, $\epsilon_{i^+}$ and $\dot{\epsilon}_{i^+}$ are respectively the strain and the strain rate in the segment $_{i^+}$. It is important to stress that the constraints imposed over the rate and the strain rate makes the line only engaged in tension. The model herein used also does not account for bending and torsional stiffness that may be important to model more complex classes of mooring devices.

### B.3. External forces

The MoorDyn library implements the effects of the line motion in still water by applying the hydrodynamic drag forces, which are solely proportional to the absolute node velocity $\dot{\boldsymbol{r}}_i$. The virtual geometry of each segment interacting with water is considered cylindrical and fully rigid. The transverse load on the line is calculated by using the approach proposed by [87], which yields:

$$\boldsymbol{D}_{t,i} = -\frac{1}{2}\rho_w \pi d l C_{dt} \|(\dot{\boldsymbol{r}}_i \cdot \hat{\boldsymbol{t}}_i)\hat{\boldsymbol{t}}_i\|(\dot{\boldsymbol{r}}_i \cdot \hat{\boldsymbol{t}}_i)\hat{\boldsymbol{t}}_i, \tag{26}$$

$$\boldsymbol{D}_{trans,i} = \frac{1}{2}\rho_w d l C_{dn} \|(\dot{\boldsymbol{r}}_i \cdot \hat{\boldsymbol{t}}_i)\hat{\boldsymbol{t}}_i - \dot{\boldsymbol{r}}_i\|((\dot{\boldsymbol{r}}_i \cdot \hat{\boldsymbol{t}}_i)\hat{\boldsymbol{t}}_i - \dot{\boldsymbol{r}}_i), \tag{27}$$

where $C_{dt}$ and $C_{dn}$ are the tangential and the transverse drag coefficients, respectively.

The added mass force at each node, when considering the tangential and the transverse contributions, can be expressed as:

$$\boldsymbol{m}_{a,i} = \rho_w Al[C_{an}(\boldsymbol{I} - \hat{\boldsymbol{t}}_i\hat{\boldsymbol{t}}_i^T) + C_{at}\hat{\boldsymbol{t}}_i\hat{\boldsymbol{t}}_i^T], \tag{28}$$

where $C_{an}$ is the added mass coefficient in the transverse direction, $C_{at}$ is the tangential added mass coefficient, $\boldsymbol{I}$ is the $3 \times 3$ identity matrix.

### B.4. Mass and integration

The second-order system of equations that accounts for the mooring line dynamic can be written as follows:

$$\begin{aligned}(\boldsymbol{m}_i + \boldsymbol{m}_{a,i})\ddot{\boldsymbol{r}}_i = \boldsymbol{T}_{i^+} - \boldsymbol{T}_{i^-} + \boldsymbol{C}_{i^+} - \boldsymbol{C}_{i^-} + \boldsymbol{W}_i + \boldsymbol{D}_{t,i} + \\ + \boldsymbol{D}_{trans,i} \text{ for } i = 2...N,\end{aligned} \tag{29}$$

where $\boldsymbol{m}_i = Al\rho\boldsymbol{I}$. The system is closed by the boundary conditions given at the cable-end nodes (fairleads or fixed), which represent the interfaces over which the MoorDyn library and the DualSPHysics code communicate. In fact, as it is shown in [58], the coupling sets a cosimulating environment, where two simulations run in separate tasks. MoorDyn+ solves the $3(N + 1)$ equations using a constant-time-step second-order Runge–Kutta integrator.

### B.5. Stability and segment damping

One of the main drawbacks of the lumped-mass approach to model cable in general is the introduction of higher modes of vibration along the axis of the line, which may give rise to nonphysical node oscillation. This problem is worked around in the formulation presented in [34] by finely setting the value $C_{int}$ that can damp out components with frequencies close to the smallest one. The phenomenon has a natural frequency defined as:

$$f_n = \frac{1}{\pi l}\sqrt{\frac{E}{\rho}}. \tag{30}$$

Eq. (30) shows that the natural frequency depends on the user defined parameter $N$, being $l = L_0/N$. The radicand only accounts for the material being modeled that for the case of polyester fiber ($E \approx 1$ GPa and $\rho \approx 1000$ kg/m$^3$) yields to $f_n \cong 10/l$ Hz. This segment vibration is hence damped out by introducing a line internal damping ($B$ [N s]) that almost makes the system critically damped ($\xi$ close to 1) at $f_n$ and it can be obtained through:

$$B = \xi l\sqrt{E\rho}. \tag{31}$$

The numerical treatment that is deployed to avoid having the line response dominated by resonance generated by the discretization could have an impact on the dynamics of interest if the dominant frequencies are close to $f_n$.

## References


[1] Falcão AFdO. Wave energy utilization: A review of the technologies. Renew Sustain Energy Rev 2010;14(3):899–918. http://dx.doi.org/10.1016/j.rser.2009.11.003.

[2] Li Y, Yu Y-H. A synthesis of numerical methods for modeling wave energy converter-point absorbers. Renew Sustain Energy Rev 2012;16(6):4352–64. http://dx.doi.org/10.1016/j.rser.2011.11.008, URL: https://www.sciencedirect.com/science/article/pii/S1364032111005351.

[3] Gomes RP, Gato LM, Henriques JC, Portillo JC, Howey BD, Collins KM, Hann MR, Greaves DM. Compact floating wave energy converters arrays: Mooring loads and survivability through scale physical modelling. Appl Energy 2020;280:115982. http://dx.doi.org/10.1016/j.apenergy.2020.115982, URL: https://www.sciencedirect.com/science/article/pii/S030626192031429X.

[4] Muliawan MJ, Karimirad M, Gao Z, Moan T. Extreme responses of a combined spar-type floating wind turbine and floating wave energy converter (STC) system with survival modes. Ocean Eng 2013;65:71–82. http://dx.doi.org/10.1016/j.oceaneng.2013.03.002, URL: https://www.sciencedirect.com/science/article/pii/S002980181300111X.

[5] Göteman M, Giassi M, Engström J, Isberg J. Advances and challenges in wave energy park optimization—A review. Front Energy Res 2020;8:26. http://dx.doi.org/10.3389/fenrg.2020.00026, URL: https://www.frontiersin.org/article/10.3389/fenrg.2020.00026.

[6] Clemente D, Rosa-Santos P, Taveira-Pinto F. On the potential synergies and applications of wave energy converters: A review. Renew Sustain Energy Rev 2021;135:110162. http://dx.doi.org/10.1016/j.rser.2020.110162, URL: https://www.sciencedirect.com/science/article/pii/S1364032120304536.

[7] Penalba M, Davidson J, Windt C, Ringwood JV. A high-fidelity wave-to-wire simulation platform for wave energy converters: Coupled numerical wave tank and power take-off models. Appl Energy 2018;226:655–69. http://dx.doi.org/10.1016/j.apenergy.2018.06.008, URL: https://www.sciencedirect.com/science/article/pii/S0306261918308754.

[8] Coe RG, Ahn S, Neary VS, Kobos PH, Bacelli G. Maybe less is more: Considering capacity factor, saturation, variability, and filtering effects of wave energy devices. Appl Energy 2021;291:116763. http://dx.doi.org/10.1016/j.apenergy.2021.116763, URL: https://www.sciencedirect.com/science/article/pii/S0306261921002701.

[9] Lavidas G, Blok K. Shifting wave energy perceptions: The case for wave energy converter (WEC) feasibility at milder resources. Renew Energy 2021;170:1143–55. http://dx.doi.org/10.1016/j.renene.2021.02.041, URL: https://www.sciencedirect.com/science/article/pii/S0960148121002093.

[10] Coe RG, Bacelli G, Forbush D. A practical approach to wave energy modeling and control. Renew Sustain Energy Rev 2021;142:110791. http://dx.doi.org/10.1016/j.rser.2021.110791, URL: https://www.sciencedirect.com/science/article/pii/S1364032121000861.

[11] Garcia-Teruel A, DuPont B, Forehand DI. Hull geometry optimisation of wave energy converters: On the choice of the objective functions and the optimisation formulation. Appl Energy 2021;298:117153. http://dx.doi.org/10.1016/j.apenergy.2021.117153, URL: https://www.sciencedirect.com/science/article/pii/S0306261921005845.

[12] Cummins W. The impulse response function and ship motions. David Taylor model basin reports, Department of the Navy: Hydromechanics Laboratories; 1962.

[13] Beatty SJ, Hall M, Buckham BJ, Wild P, Bocking B. Experimental and numerical comparisons of self-reacting point absorber wave energy converters in regular waves. Ocean Eng 2015;104:370–86. http://dx.doi.org/10.1016/j.oceaneng.2015.05.027, URL: https://www.sciencedirect.com/science/article/pii/S0029801815002115.

[14] Penalba M, Kelly T, Ringwood J. Using NEMOH for modelling wave energy converters: A comparative study with WAMIT. In: 12th European wave and tidal energy conference (EWTEC). 2017, URL: http://mural.maynoothuniversity.ie/12466/.

[15] Rahmati M, Aggidis G. Numerical and experimental analysis of the power output of a point absorber wave energy converter in irregular waves. Ocean Eng 2016;111:483–92. http://dx.doi.org/10.1016/j.oceaneng.2015.11.011, URL: https://www.sciencedirect.com/science/article/pii/S0029801815006241.

[16] Davidson J, Giorgi S, Ringwood JV. Linear parametric hydrodynamic models for ocean wave energy converters identified from numerical wave tank experiments. Ocean Eng 2015;103:31–9. http://dx.doi.org/10.1016/j.oceaneng.2015.04.056, URL: https://www.sciencedirect.com/science/article/pii/S0029801815001432.

[17] van Rij J, Yu Y-H, Guo Y, Coe RG. A wave energy converter design load case study. J Mar Sci Eng 2019;7(8). http://dx.doi.org/10.3390/jmse7080250, URL: https://www.mdpi.com/2077-1312/7/8/250.

[18] Det Norske Veritas. Recommended practice: Environmental conditions and environmental loads. Oslo, Norway: DNV; 2007.

[19] Romano A, Bellotti G, Briganti R, Franco L. Uncertainties in the physical modelling of the wave overtopping over a rubble mound breakwater: The role of the seeding number and of the test duration. Coast Eng 2015;103:15–21. http://dx.doi.org/10.1016/j.coastaleng.2015.05.005, URL: http://www.sciencedirect.com/science/article/pii/S0378383915000915.

[20] Boccotti P. Idraulica marittima. UTET univertità; 2004.

[21] Gulvanessian H, Calgaro J-A, Holický M, Gulvanessian H. Designers' guide to eurocode: Basis of structural design. 2nd ed.. ICE Publishing; 2012, http://dx.doi.org/10.1680/bsd.41714, URL: https://www.icevirtuallibrary.com/doi/abs/10.1680/bsd.41714. arXiv:https://www.icevirtuallibrary.com/doi/pdf/10.1680/bsd.41714,

[22] Trueworthy A, DuPont B. The wave energy converter design process: Methods applied in industry and shortcomings of current practices. J Mar Sci Eng 2020;8(11). http://dx.doi.org/10.3390/jmse8110932, URL: https://www.mdpi.com/2077-1312/8/11/932.

[23] Coe R, Bacelli G, Wilson D, Patterson D. System identification of a heaving point absorber: Design of experiment and device modeling. Energies 2017;10:472. http://dx.doi.org/10.3390/en10040472.

[24] Penalba M, Giorgi G, Ringwood JV. Mathematical modelling of wave energy converters: A review of nonlinear approaches. Renew Sustain Energy Rev 2017;78:1188–207. http://dx.doi.org/10.1016/j.rser.2016.11.137.

[25] Sjökvist L, Wu J, Ransley E, Engström J, Eriksson M, Göteman M. Numerical models for the motion and forces of point-absorbing wave energy converters in extreme waves. Ocean Eng 2017;145:1–14. http://dx.doi.org/10.1016/j.oceaneng.2017.08.061, URL: https://www.sciencedirect.com/science/article/pii/S002980181730505X.

[26] Ropero-Giralda P, Crespo AJ, Tagliafierro B, Altomare C, Domínguez JM, Gómez-Gesteira M, Viccione G. Efficiency and survivability analysis of a point-absorber wave energy converter using DualSPHysics. Renew Energy 2020;162:1763–76. http://dx.doi.org/10.1016/j.renene.2020.10.012, URL: http://www.sciencedirect.com/science/article/pii/S0960148120315780.

[27] Lin Z, Chen H, Qian L, Ma Z, Causon D, Mingham C. Simulating focused wave impacts on point absorber wave energy converters. Proc Inst Civ Eng - Eng Comput Mech 2021;174(1):19–31. http://dx.doi.org/10.1680/jencm.19.00038, arXiv:https://doi.org/10.1680/jencm.19.00038.

[28] Katsidoniotaki E, Nilsson E, Rutgersson A, Engström J, Göteman M. Response of point-absorbing wave energy conversion system in 50-years return period extreme focused waves. J Mar Sci Eng 2021;9(3). http://dx.doi.org/10.3390/jmse9030345, URL: https://www.mdpi.com/2077-1312/9/3/345.

[29] Davidson J, Costello R. Efficient nonlinear hydrodynamic models for wave energy converter design—A scoping study. J Mar Sci Eng 2020;8(1). http://dx.doi.org/10.3390/jmse8010035, URL: https://www.mdpi.com/2077-1312/8/1/35.

[30] Windt C, Davidson J, Ringwood JV. High-fidelity numerical modelling of ocean wave energy systems: A review of computational fluid dynamics-based numerical wave tanks. Renew Sustain Energy Rev 2018;93:610–30. http://dx.doi.org/10.1016/j.rser.2018.05.020, URL: https://www.sciencedirect.com/science/article/pii/S1364032118303629.

[31] Domínguez J, Fourtakas G, Altomare C, Canelas R, Tafuni A, García Feal O, Martínez-Estévez I, Mokos A, Vacondio R, Crespo A, Rogers B, Stansby P, Gómez-Gesteira M. DualSPHysics: from fluid dynamics to multiphysics problems. Comput Part Mech 2021. http://dx.doi.org/10.1007/s40571-021-00404-2.

[32] González-Cao J, Altomare C, Crespo AJC, Domínguez JM, Gómez-Gesteira M, Kisacik D. On the accuracy of DualSPHysics to assess violent collisions with coastal structures. Comput Fluids 2019;179:604–12, URL: http://dx.doi.org/10.1016/j.compfluid.2018.11.021.

[33] Tasora A, Serban R, Mazhar H, Pazouki A, Melanz D, Fleischmann J, Taylor M, Sugiyama H, Negrut D. Chrono: An open source multi-physics dynamics engine. 2016, p. 19–49. http://dx.doi.org/10.1007/978-3-319-40361-8_2.

[34] Hall M. MoorDyn user's guide. 2018, [Online]: www.matt-hall.ca/moordyn.

[35] Brito M, Canelas R, García-Feal O, Domínguez J, Crespo A, Ferreira R, Neves M, Teixeira L. A numerical tool for modelling oscillating wave surge converter with nonlinear mechanical constraints. Renew Energy 2020;146:2024–43. http://dx.doi.org/10.1016/j.renene.2019.08.034.

[36] Tagliafierro B, Montuori R, Vayas I, Ropero-Giralda P, Crespo A, Domínguez J, Altomare C, Viccione G, Gòmez-Gesteira M. A new open source solver for modelling fluid-structure interaction: case study of a point-absorber wave energy converter with a power take-off unit. In: Proceedings of the 11th international conference on structural dynamics, Athens, Greece. 2020, http://dx.doi.org/10.47964/1120.9052.21578.

[37] Ropero-Giralda P, Crespo AJC, Coe RG, Tagliafierro B, Domínguez JM, Bacelli G, Gómez-Gesteira M. Modelling a heaving point-absorber with a closed-loop control system using the DualSPHysics code. Energies 2021;14(3). http://dx.doi.org/10.3390/en14030760, URL: https://www.mdpi.com/1996-1073/14/3/760.

[38] Quartier N, Ropero-Giralda P, Domínguez JM, Stratigaki V, Troch P. Influence of the drag force on the average absorbed power of heaving wave energy converters using smoothed particle hydrodynamics. Water 2021;13(3). http://dx.doi.org/10.3390/w13030384, URL: https://www.mdpi.com/2073-4441/13/3/384.

[39] Crespo A, Altomare C, Domínguez J, González-Cao J, Gómez-Gesteira M. Towards simulating floating offshore oscillating water column converters with smoothed particle hydrodynamics. Coast Eng 2017;126:11–26. http://dx.doi.org/10.1016/j.coastaleng.2017.05.001.

[40] Quartier N, Crespo AJ, Domínguez JM, Stratigaki V, Troch P. Efficient response of an onshore oscillating water column wave energy converter using a one-phase SPH model coupled with a multiphysics library. Appl Ocean Res 2021;115:102856. http://dx.doi.org/10.1016/j.apor.2021.102856, URL: https://www.sciencedirect.com/science/article/pii/S0141118721003278.

[41] Waters R, Stålberg M, Danielsson O, Svensson O, Gustafsson S, Strömstedt E, Eriksson M, Sundberg J, Leijon M. Experimental results from sea trials of an offshore wave energy system. Appl Phys Lett 2007;90(3):034105. http://dx.doi.org/10.1063/1.2432168.

[42] Göteman M, Engström J, Eriksson M, Hann M, Ransley E, Greaves D, Leijon M. Wave loads on a point-absorbing wave energy device in extreme waves. International ocean and polar engineering conference, All Days, 2015, ISOPE-I-15-593.

[43] Hann M, Greaves D, Raby A, Howey B. Use of constrained focused waves to measure extreme loading of a taut moored floating wave energy converter. Ocean Eng 2018;148:33–42. http://dx.doi.org/10.1016/j.oceaneng.2017.10.024, URL: https://www.sciencedirect.com/science/article/pii/S0029801817306261.

[44] Engström J, Sjökvist L, Göteman M, Eriksson M, Hann M, Ransley E, Greaves M. Buoy geometry and its influence on survivability for a point absorbing wave energy converter: Scale experiment and CFD simulations. School of Engineering, Computing and Mathematics; 2017, p. 4, URL: http://hdl.handle.net/10026.1/13620.

[45] Chen W, Dolguntseva I, Savin A, Zhang Y, Li W, Svensson O, Leijon M. Numerical modelling of a point-absorbing wave energy converter in irregular and extreme waves. Appl Ocean Res 2017;63:90–105. http://dx.doi.org/10.1016/j.apor.2017.01.004, URL: https://www.sciencedirect.com/science/article/pii/S0141118716302668.

[46] Sjökvist L, Göteman M. Peak forces on a point absorbing wave energy converter impacted by tsunami waves. Renew Energy 2019;133:1024–33. http://dx.doi.org/10.1016/j.renene.2018.10.092, URL: https://www.sciencedirect.com/science/article/pii/S0960148118312953.

[47] Davidson J, Costello R. Efficient nonlinear hydrodynamic models for wave energy converter design - a scoping study. J Mar Sci Eng 2020;8:35. http://dx.doi.org/10.3390/jmse8010035.

[48] Monaghan JJ. Smoothed particle hydrodynamics. Rep Progr Phys 2005;68(8):1703–59. http://dx.doi.org/10.1088/0034-4885/68/8/r01.

[49] Monaghan JJ. Smoothed particle hydrodynamics. Annu Rev Astron Astrophys 1992;30(1):543–74. http://dx.doi.org/10.1146/annurev.aa.30.090192.002551.

[50] Wendland H. Piecewise polynomial, positive definite and compactly supported radial basis functions of minimal degree. Adv Comput Math 1995;4(1):389–96. http://dx.doi.org/10.1007/BF02123482, URL: http://sro.sussex.ac.uk/id/eprint/24323/.

[51] Molteni D, Colagrossi A. A simple procedure to improve the pressure evaluation in hydrodynamic context using the SPH. Comput Phys Comm 2009;180(6):861–72. http://dx.doi.org/10.1016/j.cpc.2008.12.004.

[52] Antuono M, Colagrossi A, Marrone S. Numerical diffusive terms in weakly-compressible SPH schemes. Comput Phys Comm 2012;183(12):2570–80. http://dx.doi.org/10.1016/j.cpc.2012.07.006, URL: http://www.sciencedirect.com/science/article/pii/S0010465512002342.

[53] Fourtakas G, Vacondio R, Domínguez J, Rogers B. Improved density diffusion term for long duration wave propagation. In: Proceedings of the international SPHERIC workshop, Harbin, China. 2020.

[54] Monaghan JJ, Cas RAF, Kos AM, Hallworth M. Gravity currents descending a ramp in a stratified tank. J Fluid Mech 1999;379:39–69. http://dx.doi.org/10.1017/S0022112098003280.

[55] Batchelor GK. An introduction to fluid dynamics. Cambridge mathematical library, Cambridge University Press; 2000, http://dx.doi.org/10.1017/CBO9780511800955.

[56] Monaghan J, Kos A, Issa N. Fluid motion generated by impact. J Waterway Port Coast Ocean Eng 2003;129(6):250–9. http://dx.doi.org/10.1061/(ASCE)0733-950X(2003)129:6(250).

[57] Canelas RB, Domínguez JM, Crespo AJ, Gómez-Gesteira M, Ferreira RM. A smooth particle hydrodynamics discretization for the modelling of free surface flows and rigid body dynamics. Int J Numer Methods Fluids 2015;78(9):581–93. http://dx.doi.org/10.1002/fld.4031.

[58] Domínguez J, Crespo A, Hall M, Altomare C, Wu M, Stratigaki V, Troch P, Cappietti L, Gómez-Gesteira M. SPH simulation of floating structures with moorings. Coast Eng 2019;153:103560. http://dx.doi.org/10.1016/j.coastaleng.2019.103560.

[59] Crespo A, Gómez-Gesteira M, Dalrymple R. Boundary conditions generated by dynamic particles in SPH methods. Comput Mater Continua 2007;5(3):173–84.

[60] Zhang F, Crespo A, Altomare C, Domínguez J, Marzeddu A, Shang S-p, Gómez-Gesteira M. DualSPHysics: A numerical tool to simulate real breakwaters. J Hydrodyn 2018;30. http://dx.doi.org/10.1007/s42241-018-0010-0.

[61] English A, Domínguez J, Vacondio R, Crespo A, Stansby P, Lind S, Chiapponi L, Gómez-Gesteira M. Modified dynamic boundary conditions (mDBC) for general purpose smoothed particle hydrodynamics (SPH): application to tank sloshing, dam break and fish pass problems. Comput Part Mech 2021. http://dx.doi.org/10.1007/s40571-021-00403-3.

[62] Liu M, Liu G. Restoring particle consistency in smoothed particle hydrodynamics. Appl Numer Math 2006;56(1):19–36. http://dx.doi.org/10.1016/j.apnum.2005.02.012, URL: https://www.sciencedirect.com/science/article/pii/S0168927405000565.

[63] Fourtakas G, Dominguez JM, Vacondio R, Rogers BD. Local uniform stencil (LUST) boundary condition for arbitrary 3-D boundaries in parallel smoothed particle hydrodynamics (SPH) models. Comput & Fluids 2019;190:346–61. http://dx.doi.org/10.1016/j.compfluid.2019.06.009.

[64] Martínez-Estévez I. MoorDynPlus. 2021, https://github.com/imestevez/MoorDynPlus. Accessed: 2021-07-27.

[65] Davidson J, Ringwood JV. Mathematical modelling of mooring systems for wave energy converters—A review. Energies 2017;10(5). http://dx.doi.org/10.3390/en10050666, URL: https://www.mdpi.com/1996-1073/10/5/666.

[66] Xu S, Wang S, Guedes Soares C. Review of mooring design for floating wave energy converters. Renew Sustain Energy Rev 2019;111:595–621. http://dx.doi.org/10.1016/j.rser.2019.05.027, URL: https://www.sciencedirect.com/science/article/pii/S1364032119303399.

[67] Canelas R, Brito M, Feal O, Domínguez J, Crespo A. Extending DualSPHysics with a differential variational inequality: modeling fluid-mechanism interaction. Appl Ocean Res 2018;76:88–97. http://dx.doi.org/10.1016/j.apor.2018.04.015.

[68] Tasora A, Anitescu M. A matrix-free cone complementarity approach for solving large-scale, nonsmooth, rigid body dynamics. Comput Methods Appl Mech Engrg 2011;200(5):439–53. http://dx.doi.org/10.1016/j.cma.2010.06.030.

[69] Hall M, Goupee A. Validation of a lumped-mass mooring line model with deepcwind semisubmersible model test data. Ocean Eng 2015;104:590–603. http://dx.doi.org/10.1016/j.oceaneng.2015.05.035, URL: https://www.sciencedirect.com/science/article/pii/S0029801815002279.

[70] Giannini G, Temiz I, Rosa-Santos P, Shahroozi Z, Ramos V, Göteman M, Engström J, Day S, Taveira-Pinto F. Wave energy converter power take-off system scaling and physical modelling. J Mar Sci Eng 2020;8(9). http://dx.doi.org/10.3390/jmse8090632, URL: https://www.mdpi.com/2077-1312/8/9/632.

[71] Altomare C, Domínguez J, Crespo A, González-Cao J, Suzuki T, Gómez-Gesteira M, Troch P. Long-crested wave generation and absorption for SPH-based DualSPHysics model. Coast Eng 2017;127:37–54. http://dx.doi.org/10.1016/j.coastaleng.2017.06.004.

[72] Gomez-Gesteira M, Rogers B, Crespo A, Dalrymple R, Narayanaswamy M, Dominguez J. Sphysics – development of a free-surface fluid solver – Part 1: Theory and formulations. Comput Geosci 2012;48:289–99. http://dx.doi.org/10.1016/j.cageo.2012.02.029.

[73] Whittaker C, Fitzgerald C, Raby A, Taylor P, Orszaghova J, Borthwick A. Optimisation of focused wave group runup on a plane beach. Coast Eng 2017;121:44–55. http://dx.doi.org/10.1016/j.coastaleng.2016.12.001, URL: https://www.sciencedirect.com/science/article/pii/S0378383916304161.

[74] Tromans PS, Anaturk AR, Hagemeijer P. A new model for the kinematics of large ocean waves-application as a design wave. International ocean and polar engineering conference, All Days, 1991, arXiv:https://onepetro.org/ISOPEIOPEC/proceedings-pdf/ISOPE91/All-ISOPE91/ISOPE-I-91-154/2004345/isope-i-91-154.pdf. ISOPE-I-91-154.

[75] Madsen OS. On the generation of long waves. J Geophys Res (1896-1977) 1971;76(36):8672–83. http://dx.doi.org/10.1029/JC076i036p08672, URL: https://agupubs.onlinelibrary.wiley.com/doi/abs/10.1029/JC076i036p08672. arXiv:https://agupubs.onlinelibrary.wiley.com/doi/pdf/10.1029/JC076i036p08672.

[76] Carpintero Moreno E, Fourtakas G, Stansby P, Crespo A. Response of the multi-float WEC M4 in focussed waves using SPH. In: Proceedings of 4th international conference on renewable energies offshore, October 2020, Lisbon, Portugal. 2020.

[77] Ransley E, Greaves D, Raby A, Simmonds D, Hann M. Survivability of wave energy converters using CFD. Renew Energy 2017;109:235–47. http://dx.doi.org/10.1016/j.renene.2017.03.003, URL: https://www.sciencedirect.com/science/article/pii/S0960148117301799.

[78] Hasselmann K, Barnett T, Bouws E, Carlson H, Cartwright D, Enke K, Ewing J, Gienapp H, Hasselmann D, Kruseman P, Meerburg A, Muller P, Olbers D, Richter K, Sell W, Walden H. Measurements of wind-wave growth and swell decay during the joint north sea wave project (JONSWAP). Deut Hydrogr Z 1973;8:1–95.

[79] Willmott CJ, Robeson SM, Matsuura K. A refined index of model performance. Int J Clim 2012;32(13):2088–94. http://dx.doi.org/10.1002/joc.2419, URL: https://rmets.onlinelibrary.wiley.com/doi/abs/10.1002/joc.2419. arXiv:https://rmets.onlinelibrary.wiley.com/doi/pdf/10.1002/joc.2419.

[80] Willmott CJ, Ackleson SG, Davis RE, Feddema JJ, Klink KM, Legates DR, O'Donnell J, Rowe CM. Statistics for the evaluation and comparison of models. J Geophy Res: Oceans 1985;90(C5):8995–9005. http://dx.doi.org/10.1029/JC090iC05p08995, URL: https://agupubs.onlinelibrary.wiley.com/doi/abs/10.1029/JC090iC05p08995. arXiv:https://agupubs.onlinelibrary.wiley.com/doi/pdf/10.1029/JC090iC05p08995.

[81] Gruwez V, Altomare C, Suzuki T, Streicher M, Cappietti L, Kortenhaus A, Troch P. Validation of RANS modelling for wave interactions with sea dikes on shallow foreshores using a large-scale experimental dataset. J Mar Sci Eng 2020;8(9). http://dx.doi.org/10.3390/jmse8090650, URL: https://www.mdpi.com/2077-1312/8/9/650.

[82] Altomare C, Tagliafierro B, Dominguez J, Suzuki T, Viccione G. Improved relaxation zone method in SPH-based model for coastal engineering applications. Appl Ocean Res 2018;81:15–33. http://dx.doi.org/10.1016/j.apor.2018.09.013, URL: https://www.sciencedirect.com/science/article/pii/S0141118718303705.

[83] Orphin J, Nader J-R, Penesis I. Size matters: Scale effects of an OWC wave energy converter. Renew Energy 2021. http://dx.doi.org/10.1016/j.renene.2021.11.121, URL: https://www.sciencedirect.com/science/article/pii/S0960148121017171.

[84] Hughes SA. Physical models and laboratory techniques in coastal engineering. World Scientific; 1993, http://dx.doi.org/10.1142/2154, URL: https://www.worldscientific.com/doi/abs/10.1142/2154. arXiv:https://www.worldscientific.com/doi/pdf/10.1142/2154.

[85] Flores P, Machado M, Silva M, Martins J. On the continuous contact force models for soft materials in multibody dynamics. Multibody Syst Dyn 2012;25:357–75. http://dx.doi.org/10.1007/s11044-010-9237-4.

[86] Sunday C, Murdoch N, Tardivel S, Schwartz SR, Michel P. Validating N-body code chrono for granular DEM simulations in reduced-gravity environments. Mon Not R Astron Soc 2020;498(1):1062–79. http://dx.doi.org/10.1093/mnras/staa2454.

[87] Morison J, Johnson J, Schaaf S. The force exerted by surface waves on piles. J Pet Technol 1950;2(05):149–54. http://dx.doi.org/10.2118/950149-G, arXiv:https://onepetro.org/JPT/article-pdf/2/05/149/2238818/spe-950149-g.pdf.